

Comprehensive Aerodynamic Analysis of PIV Measurements in the NFAC 80- by 120-ft Test Section Towards Understanding HVAB Hovering Rotor Characteristics

Manikandan Ramasamy*
Aerospace Engineer
U.S. Army Combat Capabilities Development Command
Aviation & Missile Center
Moffett Field, CA 94035

James T. Heineck
Physical Scientist
Experimental AeroPhysics Branch
NASA Ames Research Center
Moffett Field, CA 94035

Gloria K. Yamauchi
Aerospace Engineer,
Aeromechanics Office
NASA Ames Research Center
Moffett Field, CA 94035

Edward T. Schairer
Aerospace Engineer
Experimental AeroPhysics Branch
NASA Ames Research Center
Moffett Field, CA 94035

Thomas R. Norman
Aerospace Engineer
Aeromechanics Office
NASA Ames Research Center
Moffett Field, CA 94035

ABSTRACT

Stereoscopic particle image velocimetry (PIV) was used to characterize a hovering rotor wake at four collective pitch settings in the world’s largest wind tunnel test section. The PIV measurements are a subset of a comprehensive dataset acquired during the hover test of the HVAB rotor. Substantial effort was made to cross-validate PIV results with other test measurements and fluid mechanic theories to ensure accuracy in the reported HVAB dataset. Blade coning and flap bending were validated against early tip vortex locations. Tip vortex trajectory was compared against shadowgraphy results and free-jet boundaries. Tip vortex circulation was evaluated using a line-integral approach and least-squares curve-fit to a vortex model. Downwash velocity was compared against momentum theory values. Best practices were followed to correct inherent tip vortex aperiodicity. PIV-specific challenges were exacerbated by testing in a large facility, such as identifying and removing noisy vector fields caused by inadequate seeding. Towards this end, two new filtering methodologies were developed: (1) Modal Outlier Method (MOM), and (2) Projection on Phase-average (POP). Significant reduction in standard deviation was observed when outlier vector fields were removed. Lastly, inverse Betz theory was applied on PIV flow fields to relate trailed wake circulation and the sectional bound circulation. The resulting PIV-based loading distribution was used with lifting-line calculations and Helios simulations to analyze wake evolution. Blade-vortex interaction played a significant role in the airloads distribution that, in turn, affected the strength and evolution of the tip vortices themselves. The similarities and differences found among the PIV-, Helios-, and surface pressure sensor-based airloads were analyzed in detail to help plan future experiments.

NOTATION

Γ_b	bound circulation, m^2/s
Γ_{tr}	trailed circulation, m^2/s
Γ_v	vortex circulation, m^2/s
ζ	azimuth, deg
θ	angle around the vortex, deg
θ_0	collective pitch, deg
θ_x, θ_y	measurement plane inclination, deg
σ	standard deviation
Σ	Eigen =value
ψ	wake age, deg
Ω	rotor rotational speed
A	Eigenmode

c	blade chord
c_l	section lift coefficient
C_T	coefficient of thrust
r	radial coordinate, mm
r_c	core radius of the vortex, mm
r_v, x_v, y_v	vortex coordinates, mm
R	rotor radius
u_c, v_c	convection velocities, m/s
v_y	axial velocity, m/s
V_θ	vortex tangential velocity, m/s
V_{axial}	axial (downwash) velocity, m/s
V_{radial}	radial velocity, m/s
V_i	instantaneous velocity vector field
V	phase-averaged velocity vector field
w	streamwise velocity, m/s
X	time coefficient
x, y	spanwise and axial coordinates, mm
z	streamwise coordinate, mm

* This material is declared a work of the U.S. Government and is not subject to copyright protection in the United States. DISTRIBUTION STATEMENT A. Approved for public release PR2024100; distribution is unlimited. Presented at the Vertical Flight Society’s 80th Annual Forum & Technology Display, Montreal, Canada, May 7–9, 2024.

Acronyms:

B1, B4	blades 1 and 4, respectively
MOM	Modal Outlier Method
POD	Proper Orthogonal Decomposition
POP	Projection On Phase-average
SPS	Surface Pressure Sensor

INTRODUCTION

Wake characteristics play a significant role in determining the induced power, and therefore the overall performance of a rotor system. The strength and the spatial location of the root and tip vortices relative to the rotor blade (miss-distance) are important for acoustic analysis as well. From a design standpoint, rotor comprehensive analysis codes such as CAMRAD II and RCAS frequently apply semi-empirical wake/vortex models for performance prediction (Ref. 1–3). Rotor wake measurements are used to validate these models as well as high-fidelity computational fluid dynamic (CFD) simulations such as Helios (Ref. 4). A validated simulation adds confidence to the predicted design of future vertical lift (FVL) vehicles. Consequently, accurate characterization of the rotor wake has been a continuous research goal for several decades (Refs. 5–17). The present work is a part of the Hover Validation and Acoustic Baseline (HVAB) test campaign (Ref. 18) conducted jointly by the U.S. Army and NASA.

Generally, rotor wake characterization experiments attempt to address variations in configuration, blade planform, scale, and operational-envelope (Refs. 19). The variations can range from micro-size drones (Ref. 20) to full-size helicopters (scale studies) (Ref. 21), uniform loading to tip-loading distribution (planform studies - Ref. 22), single main-rotor to multi-rotor systems (compound-, coaxial-, tilt-, and tandem-rotor configurations), hovering out-of-ground effect and hovering in-ground effect, forward flight etc. Therefore, a relatively large set of wake measurements already exists for rotor systems (Refs. 5–9).

The present study differs from the existing wake measurements in three aspects. First, the Mach-scaled hover test was conducted in a large facility that is less susceptible to facility recirculation effects. Recirculation increases flow unsteadiness and alters the measured magnitudes. While outdoor facilities such as the NASA Ames Outdoor Aerodynamic Research Facility provide alternatives, they suffer from atmospheric turbulence, and uncontrolled wind effects. Simulations showed that the susceptibility to rotor recirculation and wall effects are minimal in the present experimental setup (Ref. 23, 24). Second, a comprehensive set of measurements, including PIV, were made during the HVAB test campaign. Therefore, data from one technique can be used to validate results from another technique to improve confidence in the overall dataset. Lastly, many of the other measurements can be related to PIV results through fluid mechanic theories. For example, sectional airloads play a substantial role in the overall wake formation. Therefore, lift distribution measurements with wake



Figure 1. HVAB rotor mounted in the 80- by 120-ft test section. Laser beam path and sheet expansion for conducting PIV.

measurements provide additional value to furthering the understanding of rotor performance. In these aspects, addition of PIV results to the HVAB dataset adds more value than when used independently.

The overall objectives of the paper are (1) to augment the HVAB dataset with PIV results that are reliably accurate with several cross validations among other measurements and theories, and (2) to describe a detailed procedure for all applied methodologies. The paper has three major sections. The first section describes the experimental set up. The second section provides a detailed procedure on the development and application of a global and a local criteria to filter the dataset. The purpose of the global criterion is to remove outlier vector fields that alter the mean values and artificially increase the standard deviation of the dataset. Outliers, in this study, refer to the noisy vector fields caused by inadequate seeding in the flow. The second section also involves description of the applied aperiodicity correction technique and the development of a local criterion to filter out incorrect samples of extracted tip vortex properties. The third section shows the results of applying the global and the local criteria on the measured vector field and tip vortex properties, respectively. A procedure to extract loading distribution from the measured PIV vector fields through trailed wake calculation is described as well. The paper concludes with comparison of PIV-based loading distribution with both the surface pressure sensor-based and Helios predicted airloads.

SECTION 1: EXPERIMENTAL SET UP

The present PIV work is a subset of a much larger hover test campaign conducted on a model-scale, 4-bladed, 11.08-ft diameter HVAB rotor in the NFAC 80- by 120-ft wind tunnel test section (Fig. 1). The objective of the overall test campaign was to acquire key experimental data at high quality to validate state-of-the-art analysis codes. The following set of measurements were acquired: rotor performance (balance), blade airloads (SPS), flow transition locations (thermography), blade deflections (photogrammetry), and wake geometry (shadowgraphy) for a range of tip Mach numbers and collective settings. Detailed description of the hardware, instrumentation, measurement systems, the specific test objectives, approach, and sample results were presented in Ref. 18. Considering the challenges involved (that will be discussed next) PIV was limited to one specific tip speed ($M_{tip}=0.65$) and four collective pitch conditions. Also, PIV was conducted at the end of the test campaign and the results were not included in Ref. 18.

Table 1 lists the set of PIV measurement conditions in terms of blade pitch angles, wake ages, and blade number. Phase-locked, stereoscopic, 3-component PIV measurements were made by synchronizing two 16-MP cameras and two pulsed lasers (1.4 J/pulse) with the rotor rotational frequency. Blade-to-blade differences were studied by comparing the flow field acquired at the same wake age of different blades.

An approximate scaled-down schematic of the experimental set up in the NFAC test section is shown in Fig. 2. Three sides of the test section are closed (no airway); the tunnel inlet was open for the entire HVAB test campaign, including during PIV image acquisition. Rotor coordinate system and azimuthal positions (as described in the paper) are also given. The PIV measurement plane was along the 90 deg azimuth. For comparison, shadowgraphy image plane covered both sides of the rotor along the 0-180 deg azimuth (see Fig. 2a and b).

The laser heads were placed in the Mezzanine (one floor beneath the test section as shown in Fig. 2); the beams were driven independently and combined at the region of interest (ROI). After passing through 3x beam expanders to reduce divergence, the beams were vertically propagated into the test section through a 9-inch hole in the mezzanine ceiling into the test section. The 25-mm beams entered the test section and were immediately turned 90 degrees using mirrors placed about 1-ft above the floor. The beams traveled 30-ft parallel to the floor and were again turned 90 degrees by another pair of mirrors (Fig. 1). The beams then reached the base of the rotor stand where two mirrors directed the beams upwards toward the rotor. A series of plano-concave-convex lenses were placed after the last mirror to generate light sheets of desired dimension. The entire mirror/lense assembly was mounted on an optical table and included several fine adjustment controllers (translation stages/goniometers) that enabled the best overlap between the sheets.

The cameras were mounted in the test section attic on either side of the light sheet in the forward-scattering mode (Fig. 2a).

The cameras were fitted with 400-mm focal length lenses and a 532-nm notch filter to reduce ambient light. Dual-axis Scheimpflug mounts were installed for compound off-axis focusing. The cameras used full-frame sensors (4872 x 3248 pixels); the size of each square pixel was 7.4 μm . A custom made, single-plane, double-sided target was mounted on an adjustable stand and was placed parallel to the laser light sheet during system calibration. The width of the target plate spanned from the root cut-out to 1 inch beyond the tip of the rotor blade (see Fig. 2f). The target was positioned such that the laser plane bisected the middle (along the thickness) of the calibration target. Self-calibration (using the first of the two images from both the cameras) was performed to account for the focal plane difference (laser plane vs. faces of the calibration board). The average uncertainty in converting the raw world coordinates to image plane coordinates after self-calibration was about one-tenth of one pixel.

The time between two laser pulses (Δt) was varied based on the collective pitch as well as the maximum displacement of the smoke particles found near the tip vortices. The goal was to achieve 4-5 pixel displacement; this resulted in a Δt of about 50- μs for the 8-deg collective pitch and 45, 40, and 35 μs for 10, 12, and 14 deg collective pitches, respectively. After every acquisition, correlation evaluation was conducted using a 32-pixel window to assure good signal-to-noise ratio in the resulting vector field.

Strategies to entrain seed particles in the desired ROI, i.e., a 6- by 10-ft plane that covers half the outboard blade section and about one diameter below the tip path plane may appear simple. However, when the ROI is about 40-ft above ground in an 80-ft by 120-ft test section that is 200-ft long, unique challenges must be overcome. Several pre-test evaluations were conducted by placing seeders at different locations on the floor and in the attic. After several attempts, especially those conducted when the rotor was running at the desired thrust condition (for other measurements such as transition or shadowgraph), ideal positions for the placement of the seeders were identified at 90, 180, and 300-deg azimuths around the rotor and about 50-ft from the base of the rotor stand. The nominal size of the smoke particles produced by the MDG seeders used in the study was about 0.9 micrometers.

Two hundred images pairs (realizations) per camera were acquired at each test condition. The efforts to uniformly fill the ROI with the seed particles, especially when the average time to set up and acquire data required about 5 minutes, was not practical. Consequently, many realizations were expected to be partially filled, if filled at all, with smoke particles or over-filled. Figure 3 shows a representative raw image from the upstream camera acquired at 8-deg collective. The blade was 60 degrees away from the light sheet. The seed void resulting from the centrifugal and Coriolis forces acting near the center of the tip vortex (shown in the close up view) helps identify the location of the tip vortex relative to the blade tip. As PIV relies on statistics-based pattern tracking, neither high-density smoke that saturates the images nor low-density smoke that fails to produce a pattern is useful. Controlling the seed particle density and directing the smoke to the desired location

Table 1. Test cases and relevant operating conditions.

Run	M_{tip}	Collective pitch (deg)	Blade number	Wake age (deg)
92	0.65	8	B1	0, 3, 7, 10, 15, 30, 60
92	0.65	8	B2,B3,B4	0, 15, 30, 60
95	0.65	10	B1	0, 15, 30, 60
95	0.65	10	B2	0
95	0.65	12	B1	3, 5, 10, 15, 30, 60
95	0.65	12	B2, B3, B4	0, 15, 30, 60
95	0.65	14	B1	0, 15, 30, 60
95	0.65	14	B2	0

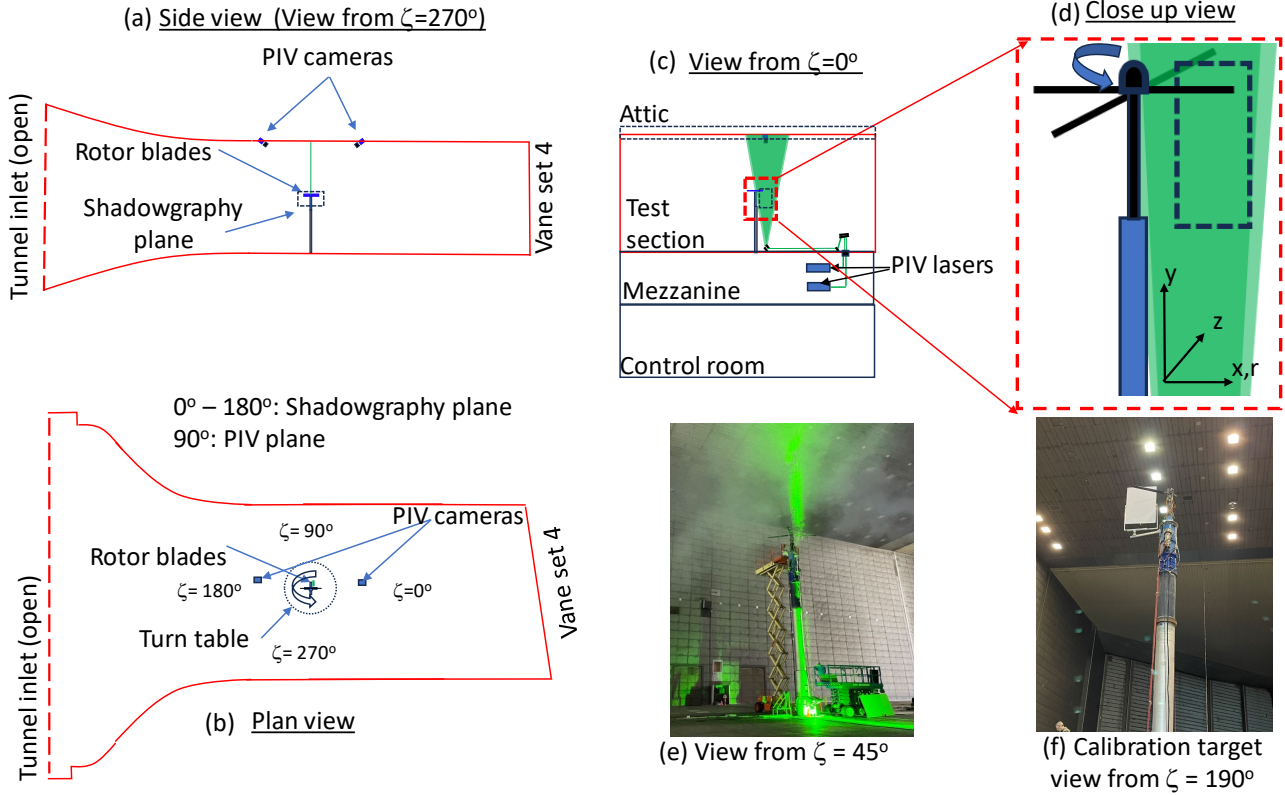


Figure 2. Experimental setup with coordinate system (not to scale).

were two of the biggest challenges in the current experiment.

The images were processed using DaVis 8.4 commercial software. A multi-step process that began with the initial interrogation window size of 64x64 pixels was reduced to a final window size of 32x32 pixels with 75% overlap. Each interrogation window produces N^2 correlation values, where N is the size of each window in terms of pixels. A vector is considered valid when the ratio of the highest two peak correlation values is larger than a threshold set by the user. In the present study, the ratio was set to 1.25 and post-processing removed vectors that fell below the threshold. Smoothing or replacing the removed vectors through interpolation was not implemented. The removed vectors created vector voids in the individual realizations. Simple phase averaging of 200 vector fields obtained at each test condition allowed qualitative visualization of the wake structure. Figure 4 shows a sample result obtained

at 8-deg collective with vorticity and out-of-plane streamwise velocity as background. Figures A1 and A2 in Appendix A show similar simple-averaged results for the 8 deg collective setting at selected wake ages. The results for the remaining cases can be found at the HVAB repository (Ref. 25). The white masked regions are blockages caused by the presence of the rotor blade between the cameras and the light sheet. Wake details such as tip vortices, vortex sheets with changing signs of streamwise vorticity (towards inboard), and the streamwise velocity excess behind the blade are all evident despite the seeding challenges.

SECTION 2: METHODOLOGY

In this section, a global criterion and a local criterion for filtering the data are assessed. The global criterion involves development of two new filters to detect and separate the outlier

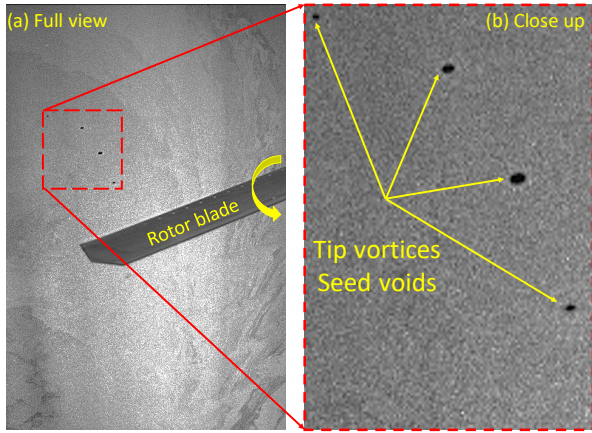


Figure 3. Representative raw image acquired at $\theta_0 = 8^\circ$, $\psi = 30^\circ$.

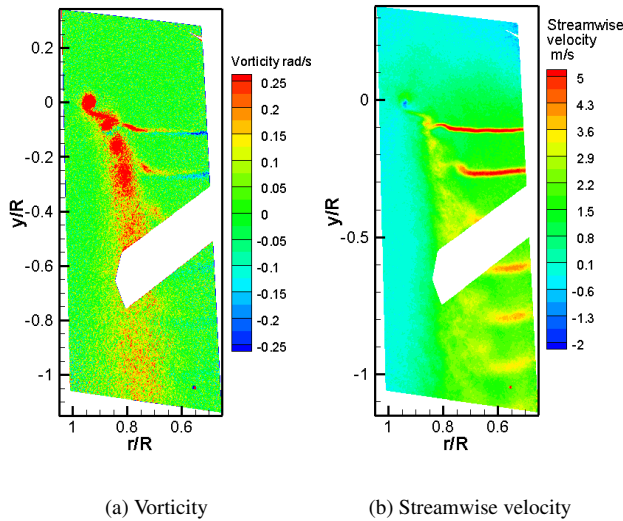


Figure 4. Representative vector field resulting from phase-averaged flow field at $\theta_0 = 8^\circ$, $\psi = 30^\circ$.

vector fields (from good vector fields) caused by the lack of optimum seeding density. The local criterion is developed and applied during the aperiodicity correction procedure while extracting tip vortex properties from within each realization. First, the development of global filters is discussed.

The primary output of PIV is planar 3-component velocity fields measured at several instances of time, also referred to as realizations. As with measurements of any flow, velocity magnitudes fluctuate because of inherent turbulence. Determining the most likely occurrence, i.e., statistical mean, requires many samples. Measuring turbulence intensity generally requires more samples than for mean quantities, and higher order shear stresses require even more samples. The present measurements results in 200 realizations (from 200 images sets), enough to calculate mean and turbulence intensities.

Except when extracting tip vortex properties, PIV vector fields are generally phase-averaged because they are often used for

qualitative and simple quantitative assessments. Examples include visualizing flow features such as tip vortices, vortex sheets or their interaction with blade/wing etc., and for determining inflow velocities, outwash, and velocity distribution across the rotor disc. Very limited reports of PIV applied for turbulence measurements are found the literature. However, flow turbulence plays an important role in the evolution of tip vortices and vortex sheets. For example, core circulation is known to be affected by turbulence in the flow (Ref. 26). Simulations that predict flow velocities apply different turbulence models for near body and far-wake (Ref. 27). Measuring turbulence intensities can, therefore, help (1) in explaining vortex evolutionary characteristics, and (2) validate the choice of applied turbulence models in simulations. Considering many future aircrafts are of multi-rotor configuration (that may also include lifting wings), the evolution of tip vortices is fundamentally important to capture the interactional effects. For example, the strength, size, and position of the tip vortex relative to the wing or the following blade can affect rotor performance (inflow variations), noise (through blade-vortex interaction), and aircraft vibration.

Turbulence intensity is the ratio of standard deviation over statistical mean. Accurate measurements of both mean and standard deviation are necessary to quantify turbulence. Therefore, substantial effort is made in this study to ensure the overall vector field represent the experimental observations in terms of statistical mean and standard deviation. The very purpose of developing global filters is to ensure the velocity field data can be used quantitatively with confidence, as well.

The problem is that PIV is based on statistics; specifically cross-correlation between two images. The signal is the laser light reflected by the seed particles (smoke) that are expected to track the flow. The signal noise comes from lack of optimum seeding density, background reflections, improper timing between the two laser pulses, smoke located between the laser light sheet and camera, etc. Non-optimum seeding density affects the signal to noise ratio of the data, alters the mean values, and artificially increases the standard deviation (turbulence intensity).

Developing a heuristic approach, therefore, is essential to separate good vector fields (produced from optimum seeding density) from the bad fields (caused by very low/high seeding density). Visual sorting of each vector field is impractical considering the number of realizations. Also, the terms *good* and *bad* are relative. A metric is needed that is not based on the measurement variable to evaluate the quality of each realization. Selecting sufficient number of high quality realizations from the acquired 200 samples at each test condition is the first objective. To achieve this goal, two new methodologies are developed and assessed: (1) Modal Outlier Method, and (2) Projection on Phase-average

Global Filter 1: Modal Outlier Method (MOM)

MOM attempts to use one of the inherent characteristics of proper orthogonal decomposition (POD) to detect outliers.

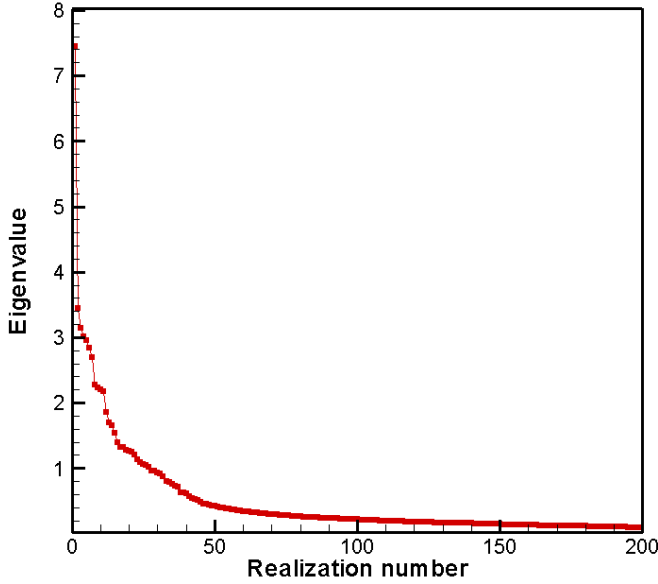


Figure 5. Eigenvalue ($\theta_0=8^\circ$, $\psi=3^\circ$).

Considering the skinny matrix that is common to PIV vector fields, snapshot POD developed by Sirovich (Ref. 28) is used.

POD decomposes a vector field into three components

$$[P] = A \Sigma X^T \quad (1)$$

where P is the mean-centered vector to be decomposed, A is the spatial Eigenmode, Σ is the Eigenvalue, and X is the time coefficient. P represents the mean subtracted 200 realizations (vector fields) acquired at each test condition. Any parameter, for example radial (u), axial (v), out-of-plane (w) velocity or their combination can be used for decomposition. While Σ represents the significance of each Eigenmode in the overall dataset, X contains the weighting parameter of each spatial mode that is required to reconstruct individual realizations. Figure 5 shows the Eigenvalue distribution for the 8-deg collective pitch and 3-deg wake age test condition.

Typically, the higher energy modes (higher eigenvalue) contribute to modeling the salient features of the flow. The lower energy modes model the turbulent fluctuations and noise. Consequently, when POD is applied to a *phase-averaged* flow field of a periodic rotor, the required number of higher energy spatial modes is less because the variations (in vortex locations, strength, or other aerodynamic features) are minimal. The eigenvalue distribution shown in Fig 5 confirms the expected distribution for periodic flows; the magnitude of the first mode is significantly higher than the other modes. The first two modes, shown in Fig. 6, also confirm that the first mode models the main features in the flow field, and the second mode models mainly noise. Modes 3 through 200 (not shown here) also looked similar to mode 2, suggesting that they are needed to model turbulence/noise as well. Taking advantage of such characteristics, it becomes possible to separate a noisy flow field caused by poor seeding from the otherwise good data set by identifying realizations that require

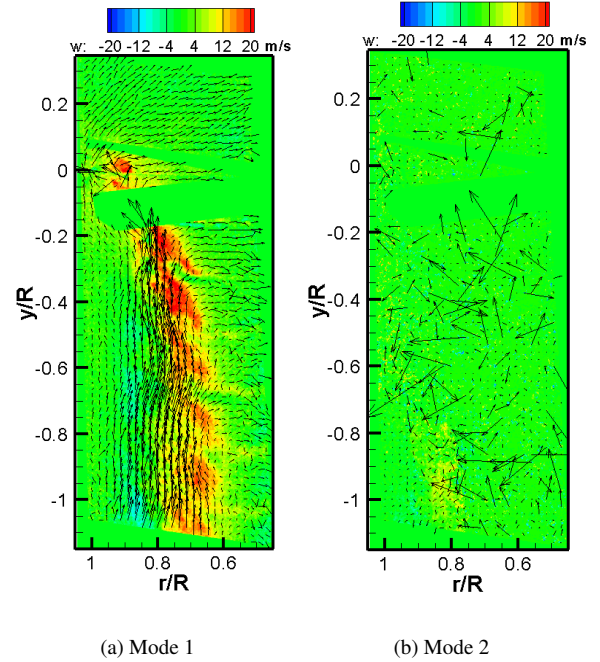


Figure 6. Two representative spatial Eigenmodes ($\theta_0=8^\circ$, $\psi=3^\circ$).

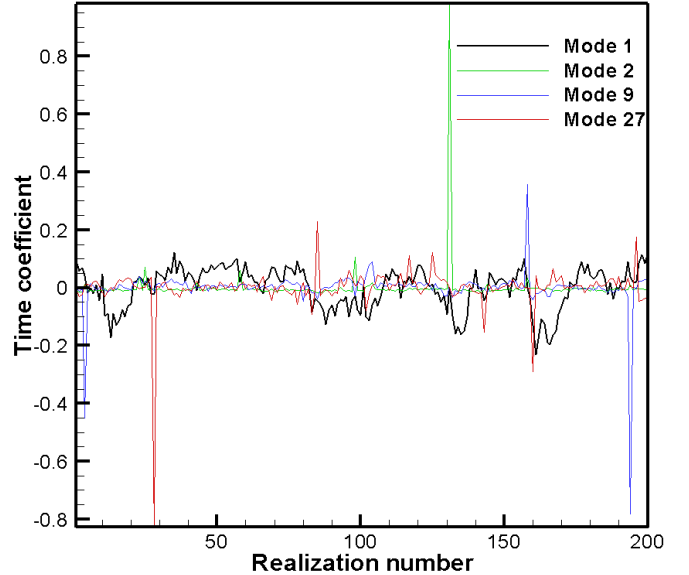
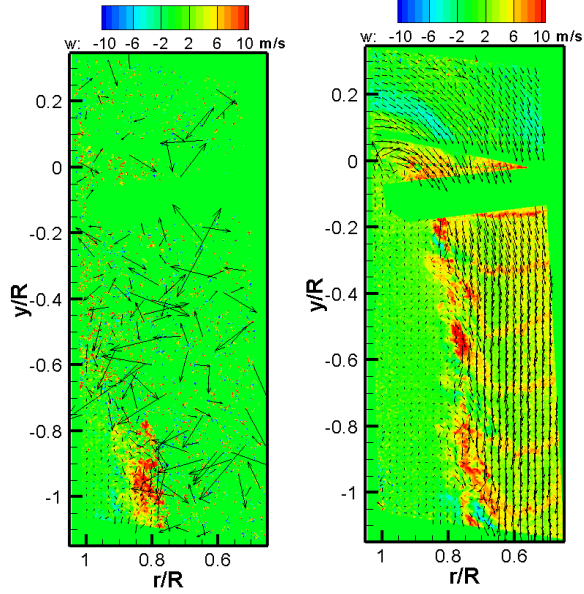


Figure 7. Few representative time coefficients ($\theta_0=8^\circ$, $\psi=3^\circ$).

higher magnitude time coefficients of lower energy modes.

The time coefficients plotted against realizations for a few selected modes, as shown in Fig. 7, are used to demonstrate the filtering methodology. The time coefficients for mode 1 are range-bound between 0.2 and -0.2, which suggests that the most of the realizations add/subtract the time coefficient-weighted mode 1 to the phase-average (mean) for reconstruction. However, modes 2, 9, and 27 have sharp peaks associated with certain realizations. For example, mode 2 shows a peak at 131. Considering mode 2 (Fig. 6b) mostly models



(a) Realization 131 (b) Realization 1

Figure 8. Two sample realizations ($\theta_0=8^\circ$, $\psi=3^\circ$).

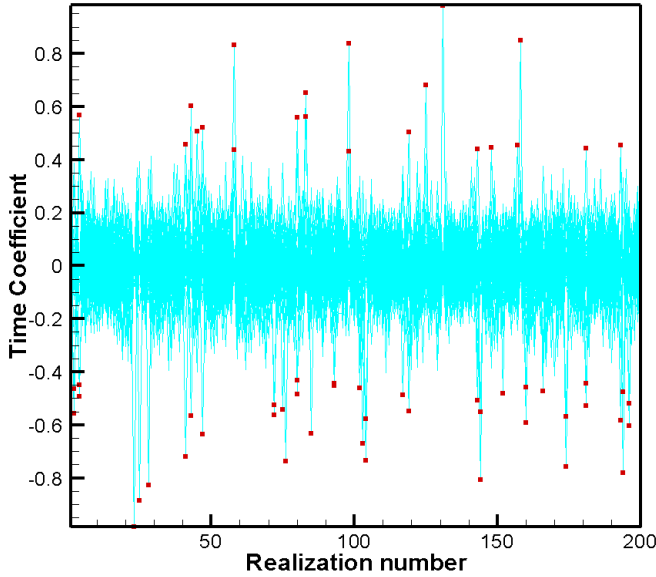


Figure 9. Selecting noisy realizations from the overall dataset ($\theta_0=8^\circ$, $\psi=3^\circ$). Realizations with red dots are deemed noisy.

noise, a high weightage (large time-coefficient magnitude) of a noisy mode implies that the data is noisy as well. As expected, realization 131 (shown in Fig. 8a) is noisy. A good realization, for comparison, is shown in Fig. 8b. Realization 1 shows all the key characteristics of the rotor wake without many erroneous vectors, as expected from an optimally seeded flow field. So, by identifying large magnitude time coefficients of noisy modes, isolating noisy vector fields is possible. Figure 9 shows the time coefficient for all the modes along with the selected high peaks. A total of 38 realizations (out of

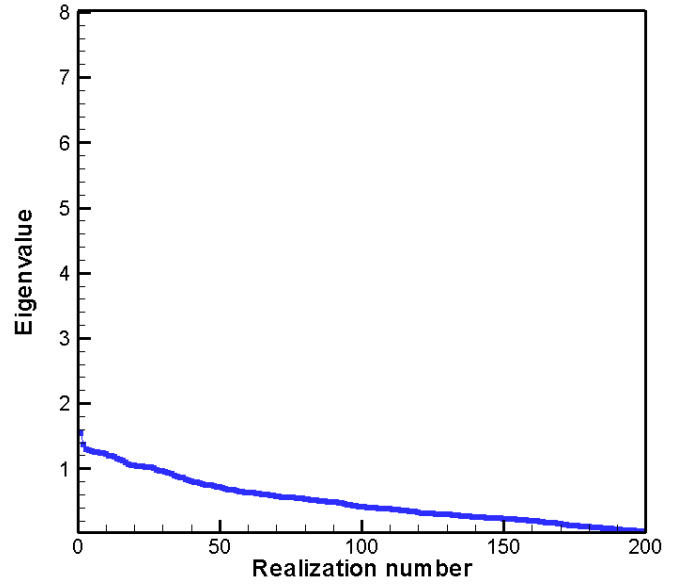


Figure 10. Eigenvalue for the test condition $\theta_0=12^\circ$, $\psi=150^\circ$.

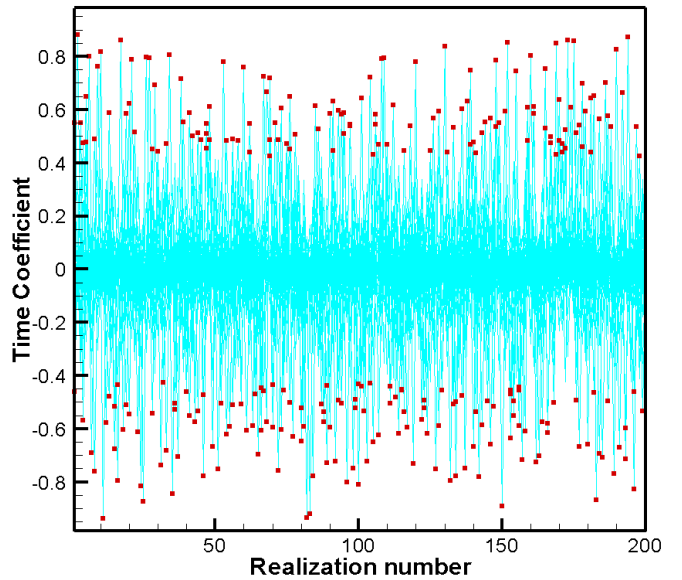


Figure 11. Selecting noisy realizations from the overall dataset ($\theta_0=12^\circ$, $\psi=150^\circ$). Realizations with red dots are deemed noisy.

200) are noisy, and can be removed from the data set.

Modal outlier method works well when the overall signal to noise (s/n) ratio (i.e., number of good vector fields vs. bad) is high. However, when the s/n is poor i.e., the number of noisy realizations is equal to or greater than good realizations, the high energy modes tend to model not only the salient features of the flow but also noise. Consequently, the advantages of using a phase-averaged periodic flow field are lost. Figure 10 shows the eigenvalue distribution for one such condition ($\theta_0=12^\circ$, $\psi=150^\circ$) where the s/n ratio is poor. The plot has the same scale as Fig. 5 for comparison. There is no distinction between high and low energy modes. When the peak-

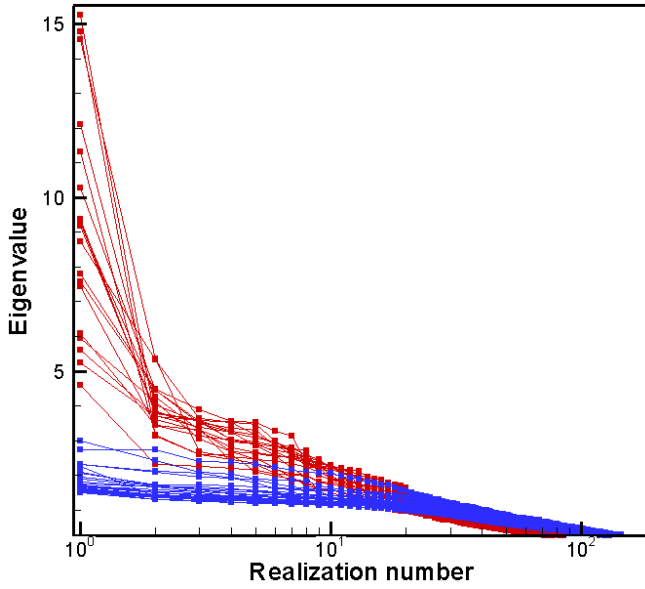


Figure 12. Eigenvalue of all test conditions.

finding algorithm (to separate noisy cycles from the dataset) is applied, 192 out of 200 cycles are selected as noisy (Fig. 11). The exaggerated rejection in the number of cycles is an inherent shortcoming of the modal outlier method when applied to a noisy data set. The fact that no single mode is dominant (and all modes model both signal and noise) means every realization requires one of the modes to be highly weighted, thus leading to rejection. Therefore, care must be taken in applying MOM filter when a clear distinction cannot be made between the modes that model salient features of the flow and noise.

The eigenvalue distributions for all the test cases listed in Table 1 is shown in Fig. 12. The x-axis is logarithmically scaled for better visualization of the higher order modes. The red and blue curves differentiate test conditions that produce a distinct first mode from the remaining modes. Overall, the modal outlier method based filtering may only be suitable for half the total number of test cases.

Global Filter 2: Projection on Phase-average (POP)

Recognizing the limitation of the MOM filter in a relatively noisy dataset, an alternative filtering methodology based on projection is assessed. Unlike MOM, which is mean-centered, POP relies on the phase-average flow field. The projection method treats the phase-average flow field as a vector (\vec{V}) with 1089x436 dimensions. All the instantaneous realizations that are vectors (V_i) of the same dimension are then projected onto the phase-average vector.

$$Proj_{\vec{V}} V_i = (V_i \cdot \vec{V}) \frac{\vec{V}}{\|\vec{V}\|^2} = \frac{V_i \cdot \vec{V}}{\|\vec{V}\|^2} \frac{\vec{V}}{\|\vec{V}\|} \quad (2)$$

The sum of projections between V_i and \vec{V} represents how much of the phase-average is embedded in each of the instantaneous vector field. Figure 13 shows the normalized sum of

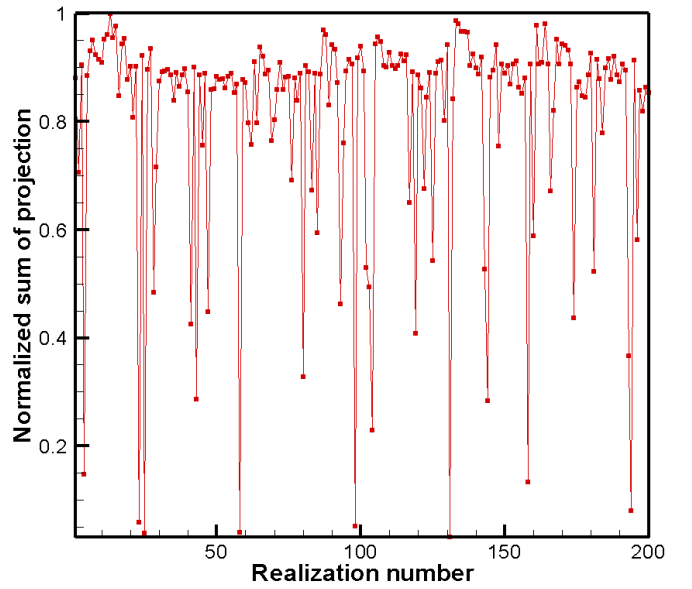


Figure 13. Projection of instantaneous realization against the phase-average vector field.

projection for each realization related to the same case discussed in the MOM filter section ($\theta = 8^\circ$, $\psi = 3^\circ$). The y-axis is normalized with the maximum sum of projection and is meant for comparison among cycles. The realization corresponding to the y-axis value of 1 is the most similar to the phase-average flow field.

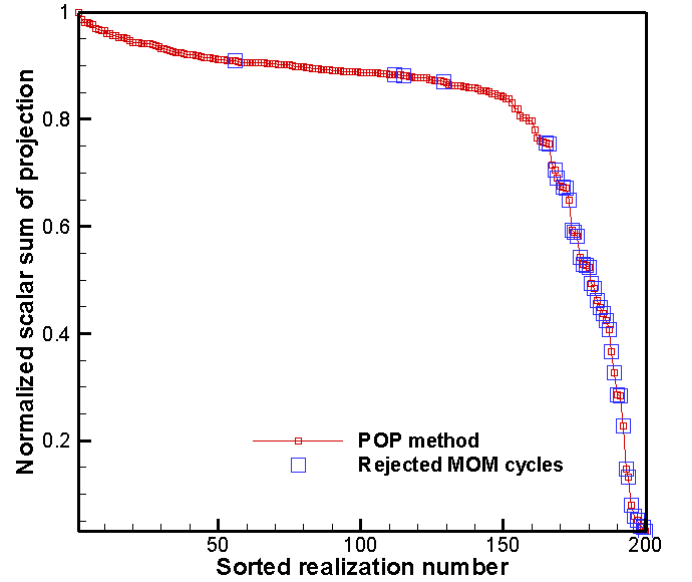


Figure 14. Ranking the realizations based on projection.

Sorting the value of the scalar sum enables the flow fields to be ranked from the best to the worst based on the similarity to the phase-average flow field. Figure 14 shows the sorted normalized scalar sum of projection for all the cycles against the sorted realizations. Such sorting shows the data quality distribution in terms of a metric and allows the user to select the number of sorted realizations for further analyses objec-

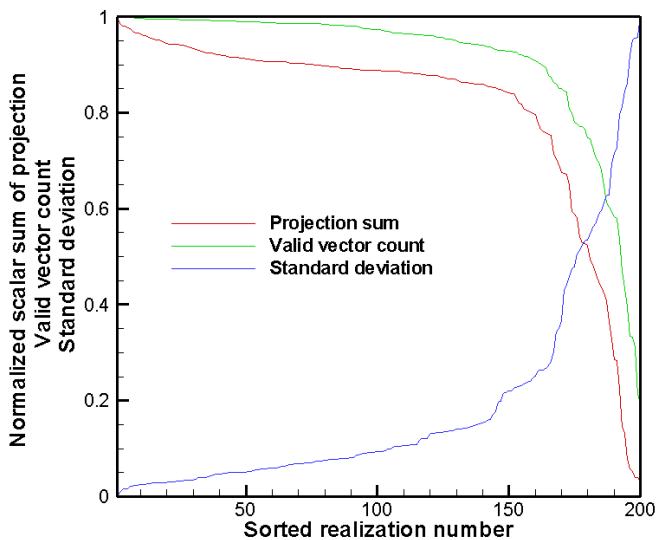


Figure 15. Valid vector count and standard deviations supports using vectorized projection sum as a filter.

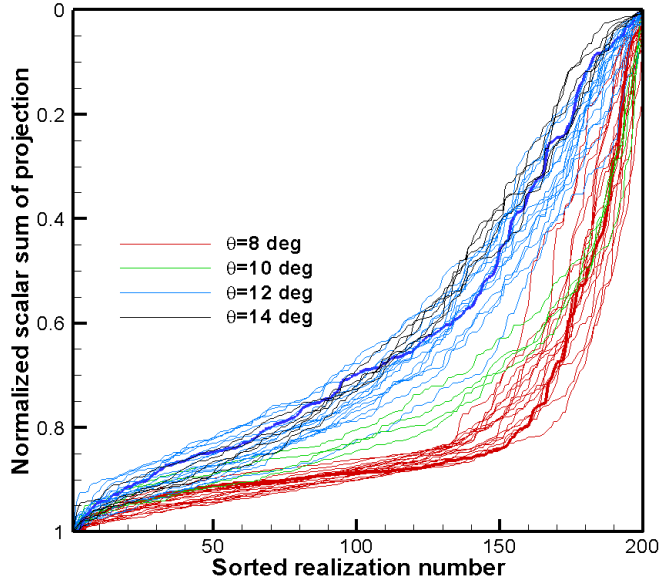


Figure 16. Relative quality of instantaneous realizations compared to the phase-average flow field.

tively. The “knee” distribution exhibited in Fig. 14 is commonly applied in cluster analysis to determine the number of clusters; the *knee* forms the boundary to separate good realizations from the bad.

For comparison, the projection values for the 38 realizations that are labeled as noisy by the MOM-based filter are also plotted in Fig. 14. Validating the POP based sorting, almost all of the rejected realizations from the MOM method are on the wrong side of the *knee* curve with low projection values.

Further validating the POP methodology is the number of valid vectors in each realization (normalized by the maximum number of valid vectors) plotted in Fig. 15. Unique to PIV, as mentioned earlier, every velocity vector in each realization carries a correlation ratio that determines the quality of the

vector. Valid vectors are those that have higher value than the threshold value defined by the user. As shown in Fig. 15, comparison of valid vector count in each realization also exhibits a *knee* in the curve (at the same sorted realization number) demarcating the good/bad realization boundary. While counting valid vectors alone can be a filtering technique for PIV applications, the distribution can change based on the threshold set by the user; hence counting valid vectors was not used as a primary filter methodology. Nevertheless, for the threshold set in the study, the results are consistent between the two methods.

Lastly, standard deviation determined from the increasing number of *sorted* realizations is plotted in Fig. 15. As expected, the standard deviation starts to increase significantly as the vectorized sum and valid vector count reduces.

The goal of the POP method is not to choose a sub-set of data that reduces the standard deviation. Every measurement exhibits fluctuations caused by inherent turbulence in the flow field, which must be accurately quantified. However, standard deviation should not be used to account for incorrect measurements caused by lack of seeding. The goal, therefore, is to quantify fluctuations caused by turbulence but remove errors that artificially increase the standard deviation. In Fig. 15, standard deviation increases gradually until about 150-160 sorted realizations, as expected, because every added realization (sorted) is farther from the phase-average than its predecessor. While the first 160 realizations contribute to about 20% of overall standard deviation, the remaining 40 realizations contribute to 80% of the standard deviation. Based on the consistency found with the valid vector count and MOM based filter, the last 40 realizations are treated as noisy and are not included from further analysis. One example of such rejected realization was shown earlier (Fig. 8a), justifying this decision.

Figure 16 shows the vectorized sum of projection for all the test cases with inverted y-axis (to visualize standard deviation). Each color represent a collective pitch setting. The two thicker lines correspond to the two cases that are used (8- and 12-deg collective pitch) as examples to demonstrate the MOM and POP techniques. Distribution of the scalar sum of projection among the various datasets exhibit the reduction of s/n ratio with increased collective. All the test cases have different *knee* locations; so a different number of sorted realizations are needed to determine the mean values and standard deviations for each case. Conservatively, a threshold value of 0.75 to 0.8 may be chosen for all datasets based on the knee defined by the 8-deg cases that have shown good seeding density. Such a decision assumes that the turbulence fluctuation magnitudes are similar among all the collective pitch settings and, in turn, will reduce the number of useful realization for high noise cases. For example, the previously analyzed 12 deg case will only use about 50 realizations out of 200.

Tip Vortex Aperiodicity Correction

Measuring tip vortex core size, peak swirl velocity, shape, spatial location relative to the blade tip, and vortex evolu-

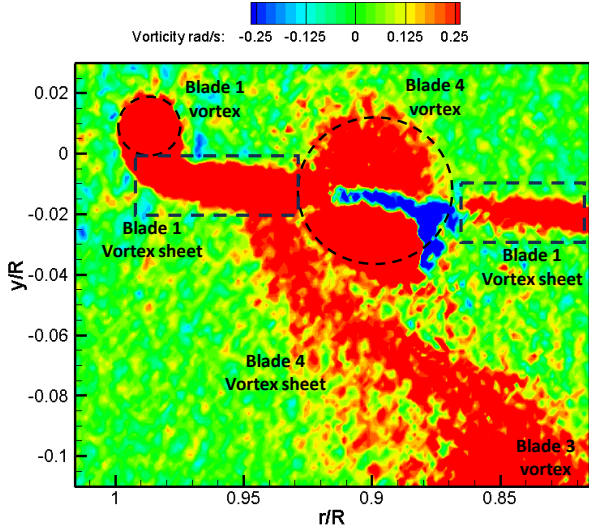


Figure 17. Components of near wake in the rotor flow field.

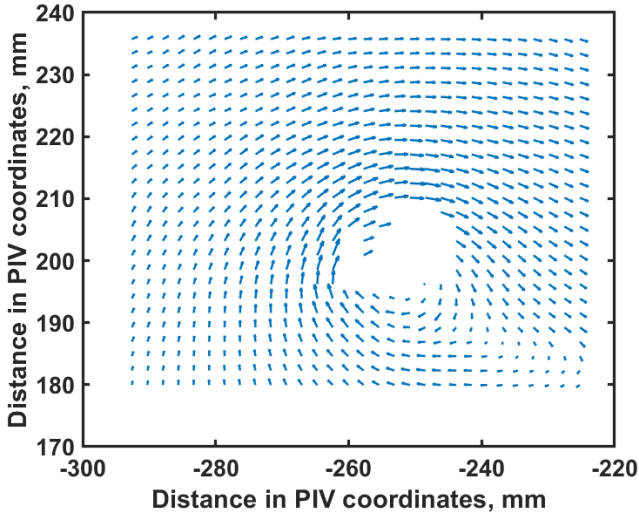


Figure 18. Sample realizations showing vector voids at the center of the tip vortex caused by seed void.

tion are typical, but important, goals when analyzing a rotor wake using PIV. One of the important hurdles in achieving the goals, which has undergone a tremendous amount of research over the past three decades, is the aperiodic nature of the tip vortex. Aperiodicity is the variation in the spatial location of the tip vortices from one cycle to another (Ref. 29). Consequently, the core size determined from a phase-averaged vector field is too large with a smeared swirl velocity profile and lower peak magnitude. Historically, two options have been proposed to accurately determine the core properties: (1) collocate the center of the instantaneous realizations and then phase-average the flow field before determining the core properties (Ref. 30,31), and (2) determine the core properties from the instantaneous realizations (Ref. 32,33). The former, while retrieving the core size correctly, cannot produce any statistical data in terms of variations in core properties. The latter, however, does provide statistical information about variations among instantaneous realizations and is used in the present

study. Choosing the aperiodicity correction method is only the first step; major challenges must be overcome and, over years, numerous methodologies have been developed to achieve the same goal. The following section starts with the primary challenge followed by a description of the methodology used in this study before discussing the wake evolution results.

The first step in correcting for tip vortex aperiodicity is identifying the vortex center for each realization. The vortex center can be the location of: (1) maximum vorticity, (2) peak axial velocity, (3) peak helicity (Ref. 31), (4) topological $\Gamma_1 \approx 1$ (Ref. 34), (5) the mid-point between the peak swirl velocity across the vortex core (Ref. 30), (6) centroid of Q-criterion (Ref. 35), and (7) least-squares fit to a mathematical/vortex model (Ref. 32,33), etc. In the case of an isolated vortex, all the above choices should produce the same result. However, helicopter tip vortices are not isolated; vortex sheets trailing from the blade stay close and roll into the tip vortices (Fig. 17). Vortices are also convecting and, often, the measurement plane is at an angle to the vortex axis. More importantly, specific to the present study, seed voids and the resulting vector voids presented a unique challenge. Among the 7 options, only the last two work reliably in the presence of a vector void.

The operational principle of PIV is imaging the laser light reflected by the smoke particles followed by cross correlation. Very close to the vortex core, centrifugal and Coriolis forces push seed particles (smoke) away from the center. The absence of seed means vector voids in all realizations. Figure 18 shows an example of a vector void. Often, interpolation is used to fill the vector voids. In the present study, however, the voids were retained because interpolation may not best represent the high-gradient flow inside a vortex.

The present study uses a vortex-fit algorithm developed by Bhagwat et al. based on least-squares fit to a vortex model (Ref. 33). The vortex function is given by

$$\mathbf{f}(r_c, \Gamma_v, x_c, y_c, u_c, v_c, \theta_x, \theta_y) = \mathbf{V}_\theta(r_v, r_c, \Gamma_v) [R_y]^T [R_x]^T \begin{Bmatrix} -\frac{y_v}{r} \\ \frac{x_v}{r} \\ r \\ 0 \end{Bmatrix} + \begin{Bmatrix} u_c \\ v_c \\ 0 \end{Bmatrix} \quad (3)$$

where the distance from the vortex center is

$$r_v = \sqrt{x_v^2 + y_v^2} \quad (4)$$

and R_x, R_y are the coordinate transformation matrices to transform data from the PIV measurement plane to the vortex plane. The corresponding angles of rotation are θ_x and θ_y . The least-squares fit attempts to reduce error in the above function with the eight independent variables, $r_c, \Gamma_v, x_c, y_c, u_c, v_c, \theta_x, \theta_y$ through finding the best match with measured velocities. Multiple vortices can be simultaneously fit; however, each vortex was fit individually in this study.

Even though all the needed vortex parameters can be obtained from the curve fit, only the identified centers were used to prevent the laminar assumption (Lamb model) to play a role in

characterizing the tip vortices as observed in the present measurements. The choice of a laminar Lamb model (Ref. 36) versus a fully turbulent Iversen model (Ref. 37) changes the ratio of core circulation to the total vortex circulation, but the centers will remain the same (Ref. 33). Once the centers are identified, vortex properties such as core size, peak swirl velocity, and core circulation were determined from each realization.

The following section describes the methodology used in this study, from identifying centers to determining vortex core properties. The MOM/POP filtering approach established that not all 200 realizations are usable. However, simply rejecting the same realizations, as earlier, may not be correct because vector properties depend largely on local velocities and the vector voids affect the results. An alternative acceptance criterion using simple fluid mechanic theories was used to separate outliers in the vortex properties.

Local Filter – Tip Vortex Property Outliers

From applying the curve fit (Ref. 33) to 200 realizations, 200 vortex centers were identified. A circular (closed-loop) line integral was then applied over a small square with the center obtained from curve-fit values and each side equaling the median diameter of the 200 curve-fit values. The size selection was later confirmed for every case to be appropriate using the circulation distribution obtained from the horizontal and vertical cuts through the vortex center. If the line-integral circulation matched the curve-fit circulation within 25%, the center values from the curve-fit sample set were accepted. Figure 19 compares the two circulations for the same 8-deg case analyzed earlier. Samples that do not meet the acceptance criterion are marked with a black square.

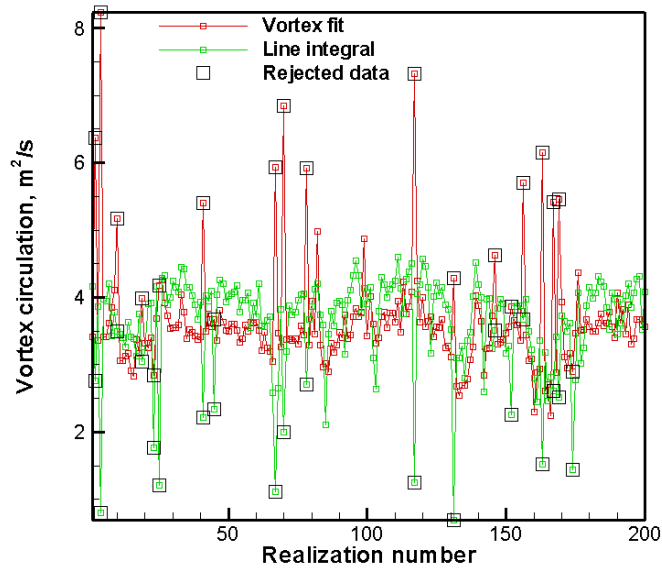


Figure 19. Comparison of vortex circulation determined using vortex fit method and line integral.

Application of the acceptance criterion is shown in Fig. 20. Vortex locations that clearly depart from the majority of the

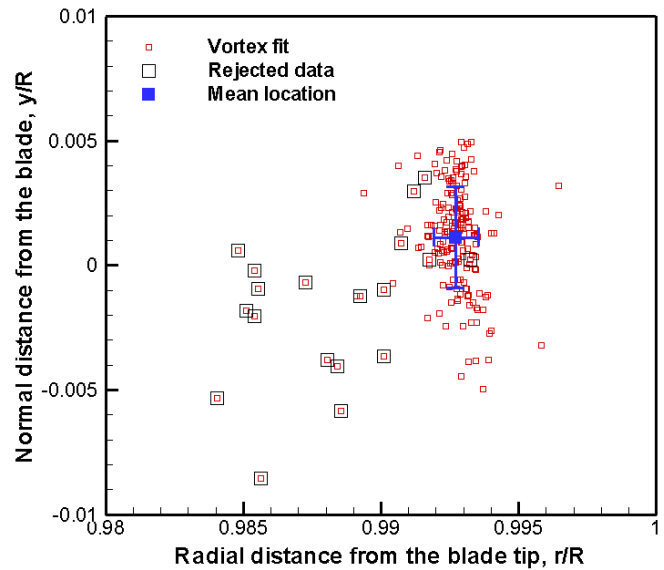


Figure 20. Vortex locations determined from individual realizations using vortex fit method, rejected data, and the resulting mean and standard deviation.

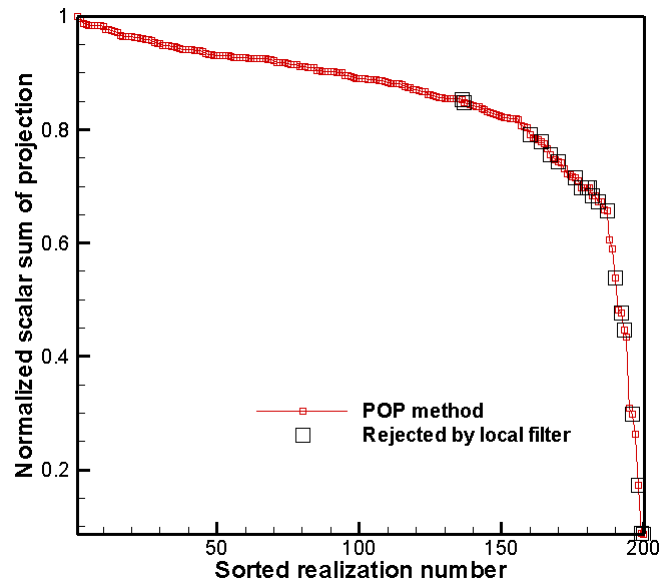
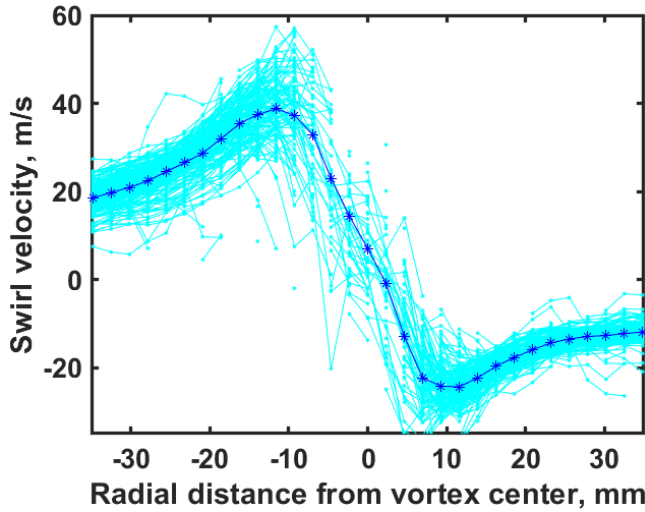
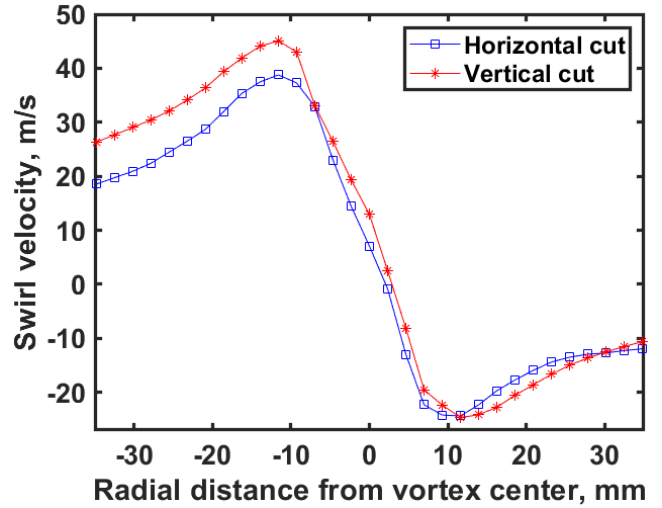


Figure 21. Realizations showing the relative rank of selected data.

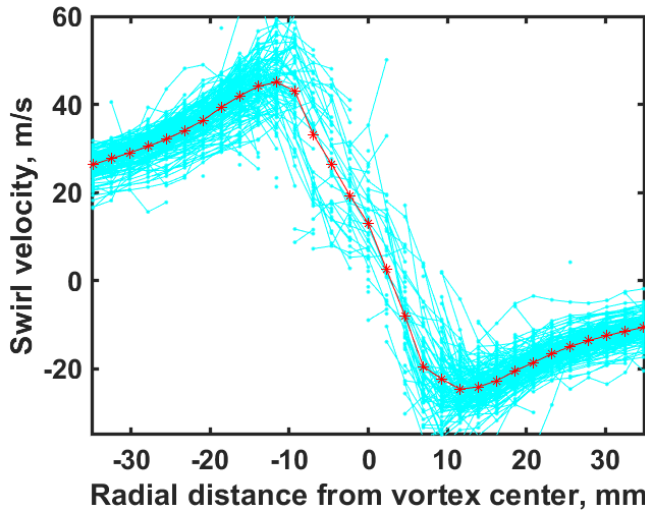
data are rejected. The difference in circulation of 25% was not random or universal among all cases. The value of 25% was the maximum and corresponds to half the circulation contained in the vortex sheet that lies between Blade 1 vortex and Blade 4 vortex in Fig. 17. The assumption is that half the section of vortex sheet rolls into the Blade 1 tip vortex and the other half into the other Blade 4 vortex. The rejection of the samples was further justified when the results were plotted against the sorted realization results obtained using the POP method in Fig. 21. Almost all the rejected samples belonged to realizations with low vectorized projection sum. As expected, a few rejected samples had high projection sum (e.g., two samples near sorted realization 140) and a few accepted



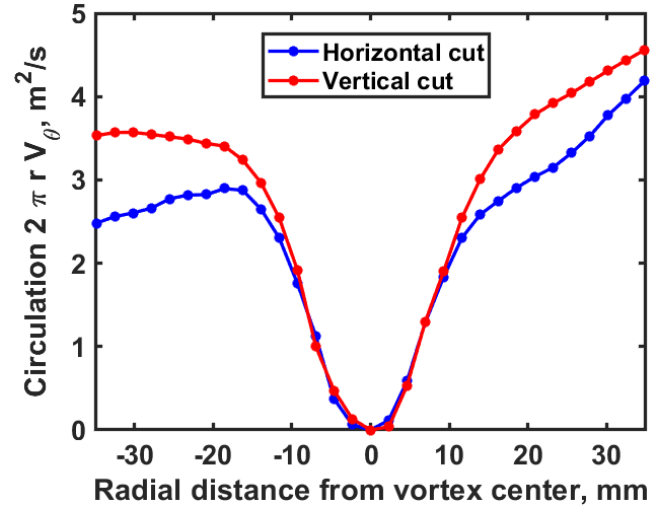
(a) Horizontal cut



(a) Centered mean swirl velocity profiles



(b) Vertical cut



(b) Circulation

Figure 22. Horizontal and vertical cuts through the center.

samples had low projection sum (sorted realization number 197). The above exceptions are examples of conditions where (1) the vector voids near the vortex center dominate the results even though the overall flow field had optimal seeding density and (2) seeding near the vortex center was better compared to the overall flow field, respectively. Overall, 180 samples were selected for extracting vortex core properties (for $\theta_0 = 8^\circ$, $\psi = 3^\circ$).

With the circulation criterion providing the necessary filter to identify and separate outliers, the focus turns to extracting vortex properties from the accepted sample set.

Historically, plots of u - and v -components of velocity along the vertical and horizontal cuts, through the vortex center were used to determine the vortex core diameter (distance between the velocity peaks). The literature shows such cuts can be

Figure 23. Mean swirl velocity and circulation distribution mean ($\theta_0 = 8^\circ$, $\psi = 3^\circ$).

made before or after collocating the vortex centers from all realizations. There is an issue, however, when vortex centers are not aligned to the measurement grid nodes. A rectification would be to interpolate all the flow fields corrected for centers onto a common grid. However, interpolated velocity magnitudes are always lower than the measured values (unless a vortex model is used), negating any benefit gained through interpolation.

Figure 22 shows the horizontal and vertical cuts made at the nearest node to the measured vortex center (from curvefit). All 180 accepted samples are plotted. The density of data points is comparatively low near the vortex center than elsewhere. Ensemble averages of the swirl velocity profiles (uncorrected for vortex convection velocity) and circulation (after

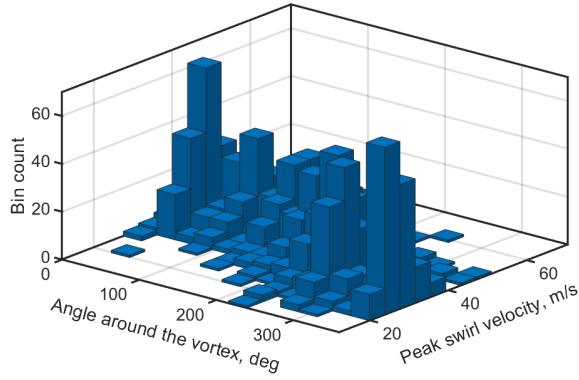
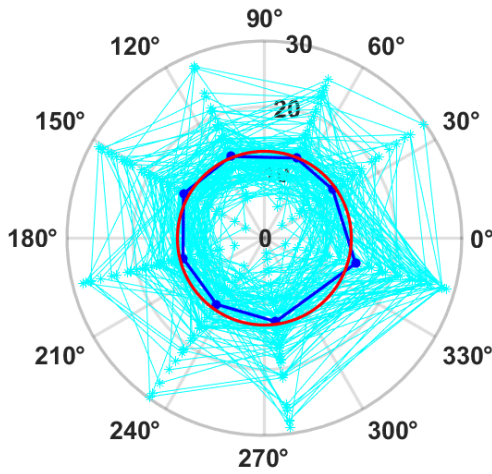
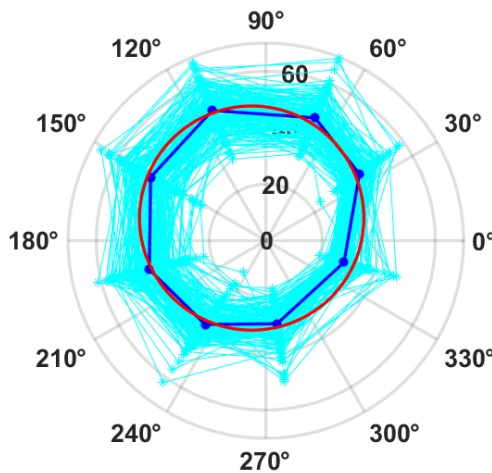


Figure 24. Histogram showing the peak swirl velocity around the vortex.



(a) Core radius, mm



(b) Peak swirl velocity, m/s

Figure 25. Core radius and swirl velocity distribution around the vortex- ($\theta_0 = 8^\circ$, $\psi = 3^\circ$).

convection velocity correction) are plotted in Fig. 23. Approximately 11 measurement nodes are inside the core, sufficient enough to resolve the vortex core size. The differences found between peak swirl velocity magnitudes and core radius for the horizontal and vertical cuts suggests evaluating the flow field around the vortex.

Evaluation of core properties using data from around the vortex (0 to 360 degree) starts with a coordinate transformation from cartesian to polar. Using the centers identified from the vortex fit (i.e., not the closest grid node), the coordinates (x and y) and the velocities (u and v) are converted to radial/azimuthal values (r and θ) and radial/tangential velocities (V_r and V_θ), respectively. All the data were then sorted into eight bins of equal size (45 degrees). Peak swirl velocity within each bin, the corresponding radial coordinate, and the angle θ were identified. Histogram of the selected peak swirl velocity around the vortex is shown in Fig. 24. The radial coordinate defines the core radius within each bin. The resulting distribution of peak swirl velocity and core radius around the vortex for each realization are shown in Fig. 25.

Two factors improved the resolution of the measurement: (1) conversion to polar coordinates, especially when the centers are not aligned to one of the grid nodes, and (2) using vectors surrounding the vortex. Data from the accepted samples are plotted in cyan, corresponding mean values are in blue, and the equivalent circle is plotted in red. The shape of the core appears circular. The peak swirl velocity is off-centered with a bias towards the upper left (about 135 degrees), which is a consequence of convection velocities at early wake ages. The bias should be around 235 degrees for later wake ages. Nevertheless, adding all velocities around the azimuth cancels the effect of convection velocity, and the red curve shows the equivalent peak swirl velocity around the vortex.

The mean core radius and peak swirl velocity measured around the vortex are 13.37 mm and 40.02 m/s, respectively. The standard deviations are about 4.37 mm and 6.40 m/s, respectively. The mean peak swirl velocity was higher than the horizontal and vertical cut by about 8-10%. The difference is expected because the binned procedure seeks peak magnitudes within a bin (spanning 45 degrees) that has higher spatial resolution than the cartesian grids ($\Delta r < \Delta x$); the horizontal/vertical cut procedures just select the highest velocity on the grid node in one direction.

Similar results were obtained for the 12-deg collective case, a relatively noisy dataset. The results from data reduction process, beginning from the acceptance criterion analysis to the final polar plots, are shown in Appendix B.

SECTION 3: RESULTS

Phase-average vector fields, tip vortex trajectories, and vortex core properties obtained at various collective pitch conditions (after applying the global filters, aperiodicity correction, and local filter) are discussed first in this section. This is followed by determining blade loading distribution from phase-average PIV vector fields.

Vector Field Statistics

Since the s/n ratio for the 8-deg case is high, the MOM filter was applied to calculate the phase-average and standard deviation. For the relatively higher noise 10-, 12-, and 14-deg cases the POP filter was applied. Phase-averages for the streamwise and axial velocity components obtained using the MOM filter for the $\theta = 8^\circ$ case is shown in Fig. 26. The benefits of applying the MOM filter are analyzed by comparing the filtered results against the all-sample statistics. For a good s/n dataset (such as the 8-deg case), no significant difference can be expected in the mean values because the number of good realizations significantly outnumber the bad realizations. As contour plots can provide biased views based on selected thresholds, a vertical cut over the entire measurement region at $r/R = 0.5$ for all three components of velocities is shown in Fig. 27. Lighter shades represent the all-sample dataset and the darker shades correspond to the filtered dataset. The streamwise velocity excess caused by the vortex sheet passage can be tracked up to 7 blade passages; the distance between the two high value peaks match the local convection velocity (axial component). The downwash (axial) velocity gradually increases from 10 m/s from above the rotor plane to about 30 m/s at one rotor radius below the rotor. As expected from a high s/n ratio dataset, no significant difference was found in the mean values between the filtered and all-sample datasets.

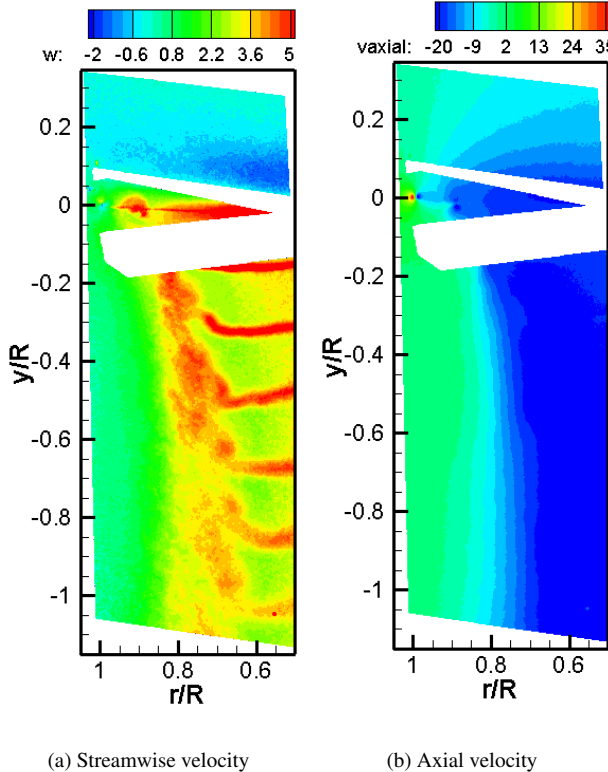


Figure 26. Phase-average flow field from MOM filtered dataset ($\theta_0 = 8^\circ$, $\psi = 3^\circ$).

Unlike the phase-average (despite a large number of good realizations) the standard deviation is different between the two datasets. An example is shown in Fig. 28 for the axial velocity

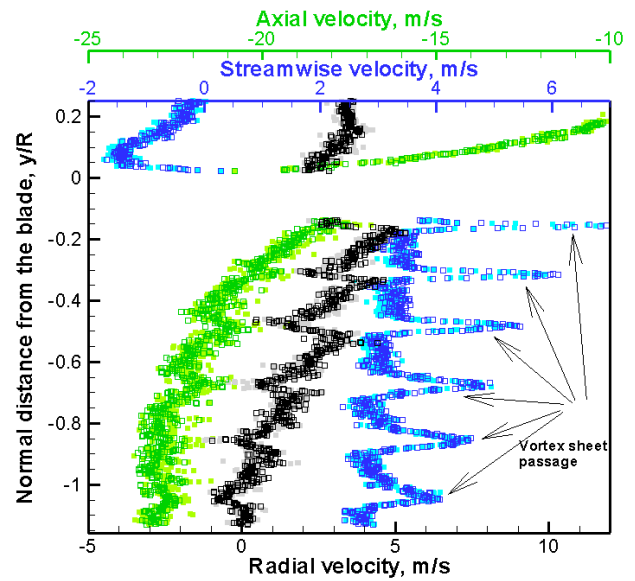


Figure 27. Phase-average velocity comparison at $r/R=0.5$ (lighter shades – all samples, darker shades - filtered data).

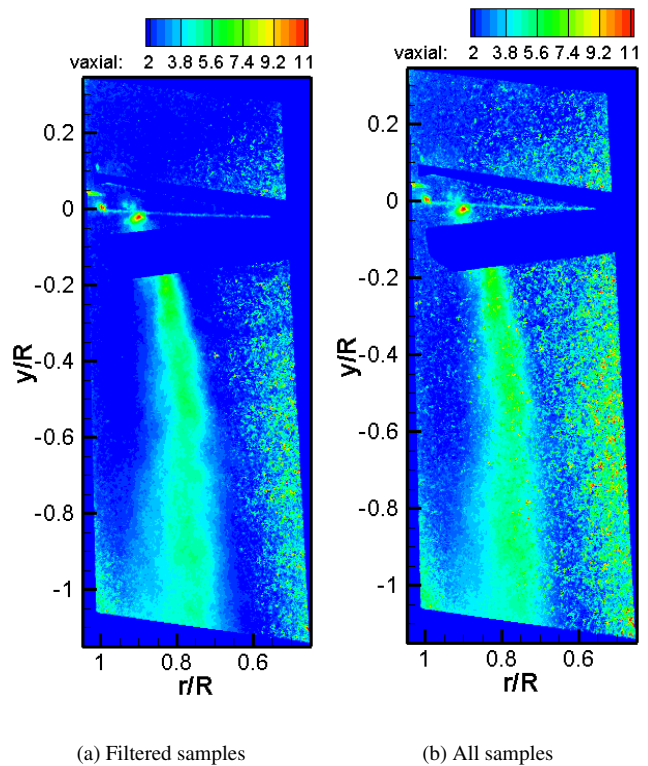
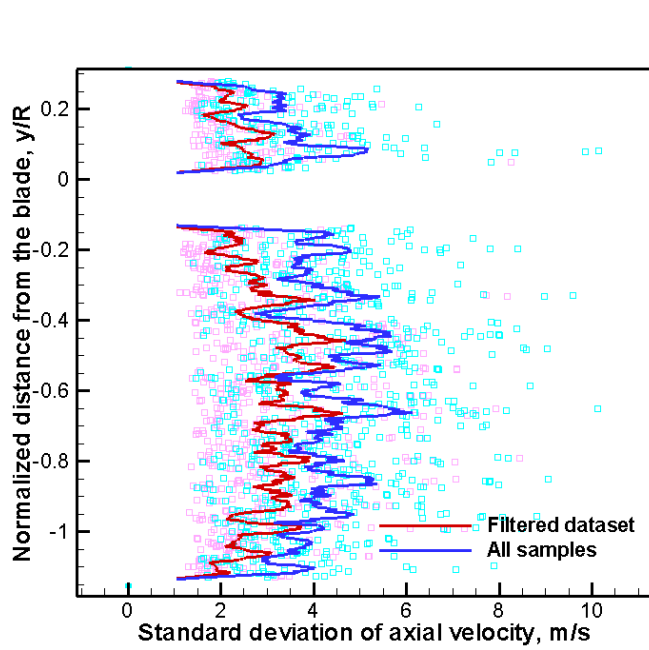
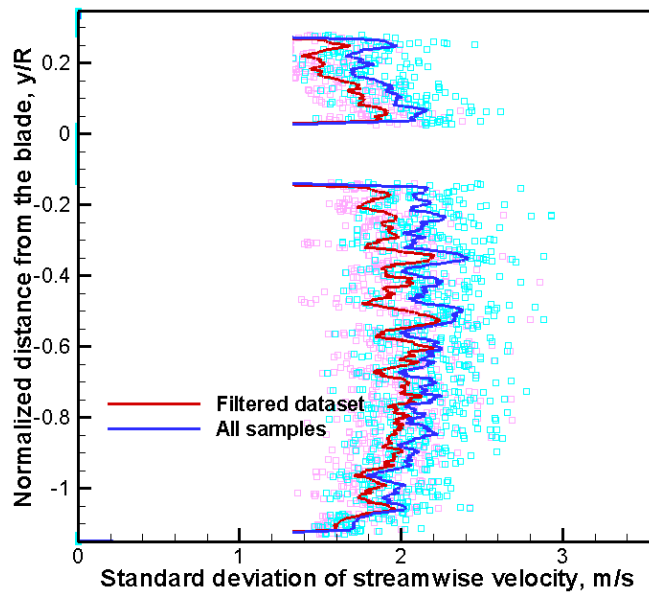


Figure 28. Comparing the standard deviation between MOM filtered data and all-sample data of axial velocity.

component. The all-sample standard deviation shows much higher magnitude than the filtered dataset, especially inboard. A similar vertical cut along $r/R = 0.5$ for standard deviation is shown in Fig. 29. The symbols represent local σ at every measurement node while the lines represent a moving average of 20 nodes. The moving average, added to smooth the chaotic variations exhibited by the individual nodes, highlights the



(a) Axial velocity

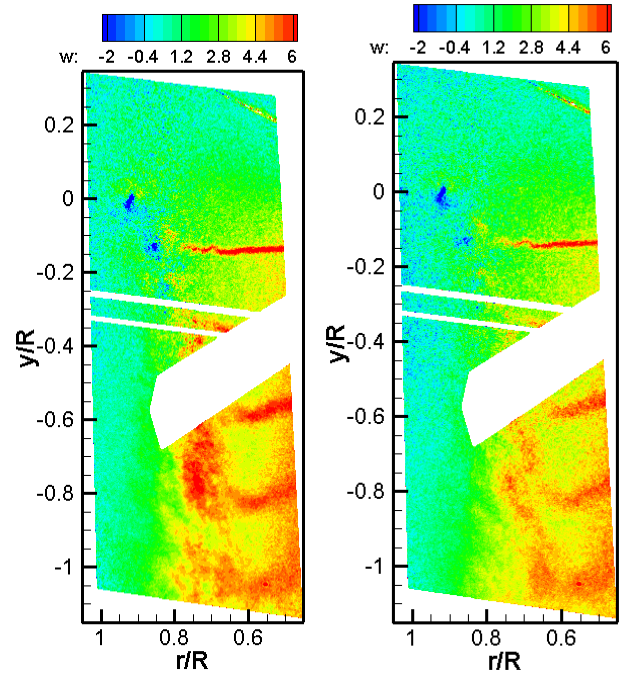


(b) Streamwise velocity

Figure 29. Comparison of standard deviation along $r/R=0.5$ between MOM filtered dataset and all-samples.

magnitude difference between the two datasets. The σ of both the axial velocity and the radial velocity (not shown) components are about 28% lower for the filtered dataset compared to the all-sample dataset. The streamwise velocity showed a difference of 9%.

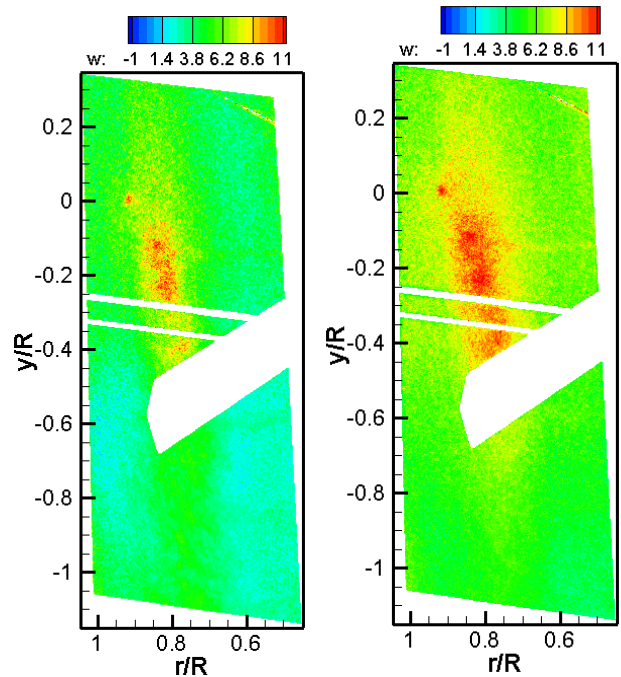
Similar comparison of all-sample phase-average and standard deviation for the low s/n ratio dataset discussed earlier ($\theta_0=12$) is shown in Figs. 30 through 32. For brevity, only streamwise velocity and axial velocity are compared. Focus-



(a) Filtered samples

(b) All samples

Figure 30. Comparison of POP-filtered (projection sum > 0.75) and all-sample phase-averages.



(a) Filtered samples

(b) All samples

Figure 31. Comparison of POP filtered (projection sum > 0.75) and all-sample standard deviation.

ing on the wake excess (in the vortex sheet), the all-sample phase average not only reduces the overall magnitude (mean) of the excess velocity but also smears out the high velocity

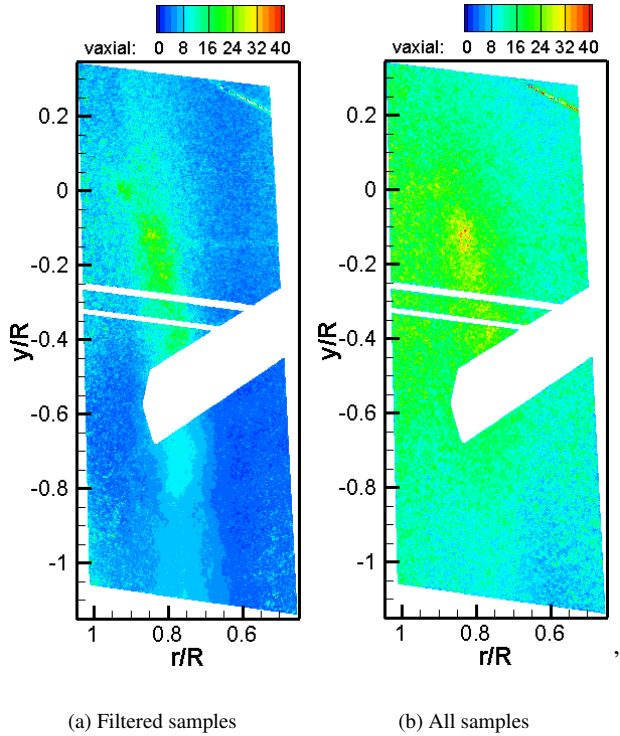


Figure 32. Comparison of standard deviation between POP filtered data (projection sum > 0.75) and all samples of axial (downwash) velocity.

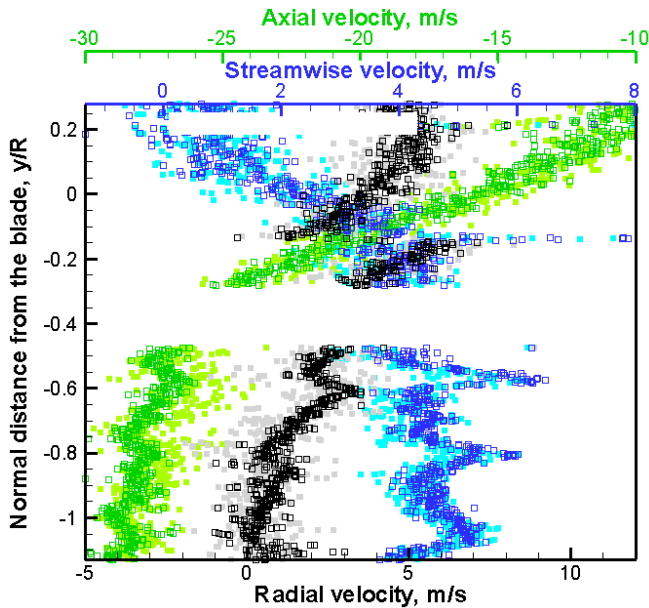
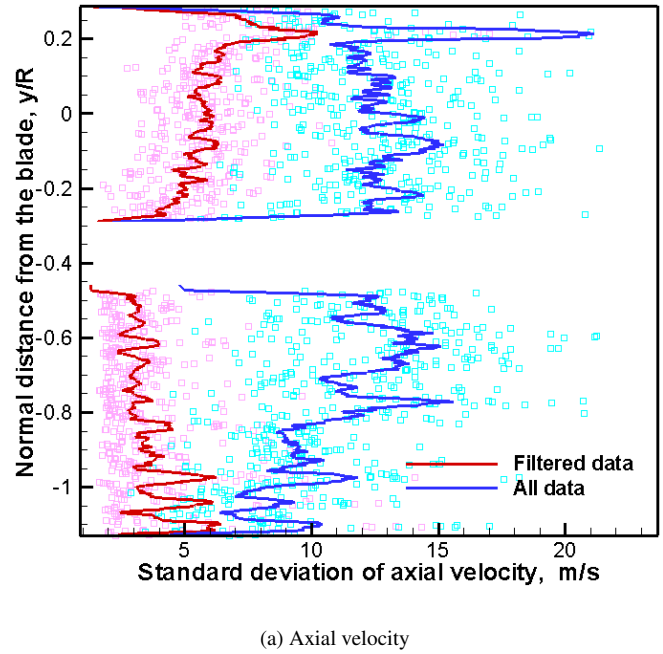
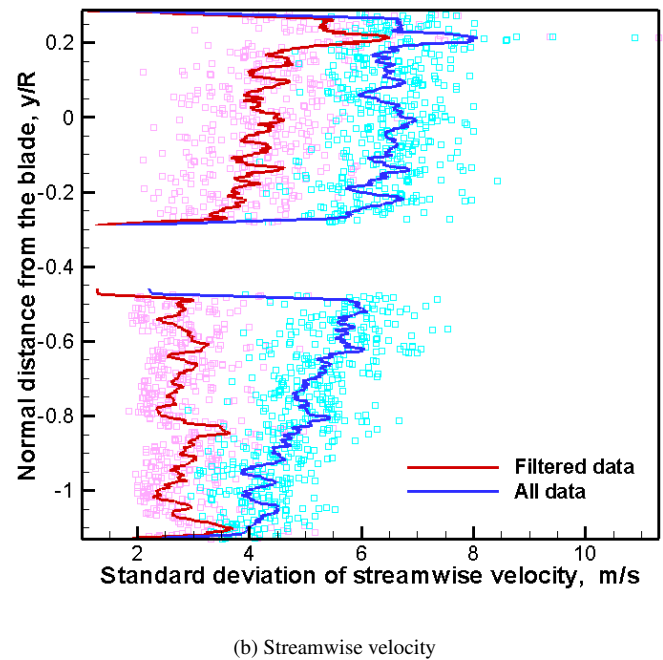


Figure 33. Phase-average velocity comparison at $r/R=0.5$ (lighter shades – all samples, darker shades - filtered data).

regions. Also, the standard deviation is generally higher over the entire flow field compared to the POP-filtered data set. The increase in fluctuation is significant not only along the vortex trajectory but also on the inboard ($r/R < 0.7$) sections of the blade. Comparison of the standard deviation for the axial (downwash) velocity shows significantly larger differences



(a) Axial velocity



(b) Streamwise velocity

Figure 34. Comparison of standard deviation along $r/R=0.5$ between POP filtered dataset and the all-sample dataset.

between the all-sample and the filtered datasets. Vertical cuts (at $r/R=0.5$), as done earlier for the 8-deg case, are also shown in Figs. 33 and 34. A reduction in magnitude of axial (downwash) velocity and a substantially higher standard deviation were found for the all-sample dataset compared to the filtered data. The σ for both the axial velocity and the radial velocity (not shown) components are about 60% and 65% lower for the POP filtered dataset compared to the all-sample dataset, respectively. The streamwise velocity σ showed a reduction

of about 37%.

As mentioned earlier, the goal is not to simply reduce standard deviation through a subjective selection of realizations but to remove incorrect vector fields (caused by poor seeding) that artificially increases the standard deviation. Representing turbulence accurately requires determination of velocity fluctuation (standard deviation) in the data caused only by turbulence in the flow. MOM and POP filtering approaches provide metrics to separate the good realizations from the bad (poorly seeded) that, in turn, results in a more accurate determination of the standard deviation.

Tip Vortex Properties

Having established the acceptance criterion and the procedure to extract tip vortex properties, the methodology was applied to all four test conditions listed in Table 1. Figure 35 shows the trajectory of tip vortices for all the 8-, 10-, 12-, and 14-deg collective pitch cases. The x- and y- axes are normalized using the radius of the blade. Figure 35 is in PIV coordinates, i.e., $y/R=0$ represents the tip of the blade at 8-deg collective. The difference in the earliest tip vortex position between 8 and 14 deg, therefore, is a measure of the combined blade coning and flap deflection. PIV measurements showed $\Delta y = 43.7$ mm. During the HVAB test campaign, blade coning was measured at the root using strain gauge and the $\Delta\beta_0$ between 8 and 14 degree cases was 1.26 deg. Similarly, the change in elastic flap bending deflection measured using photogrammetry was 10.6 mm. Adding the two effects ($R \tan(\Delta\beta_0) + 10.6$) results in 44.1 mm, a difference of 0.4 mm compared to PIV that is within the measurement resolution of the PIV grid. The values for coning (averaged over the azimuth) angle and deflection are obtained from the HVAB data website and are described in Ref. 18. Such a good correlation between the two techniques increases confidence in both the measurements as they cross-validate each other.

For the 8- and 12-deg collective pitch cases, the trajectory of tip vortices from each blade could be tracked individually. Blade-to-blade differences in the tip vortex trajectory for the 8-deg collective pitch condition are shown in Appendix C. For the 10- and 14-deg cases, measurements were made only for one quarter of a revolution. So, tip vortex locations identified for every 90-deg wake age belong to different blades. In general, as observed in many past experiments, the scatter in the x- and y- axis locations increases with wake age. Up until the first blade passage, the scatter is more in the blade normal direction compared to the radial direction. After the first blade passage, the scatter was higher in the radial direction.

The axial and radial locations (corrected for blade coning and flap bending) are plotted against wake age in Figs. 36 and 37. Data obtained from the shadowgraphy technique are also plotted in the background. Unfilled circles and crosses of the same color are used (to represent shadowgraphy data) for matching collective pitch angles between the two techniques. Two slopes can be observed in both the axial and radial trajectories and they are related to the first blade passage. The axial velocity of the tip vortices increasing after the first blade passage,

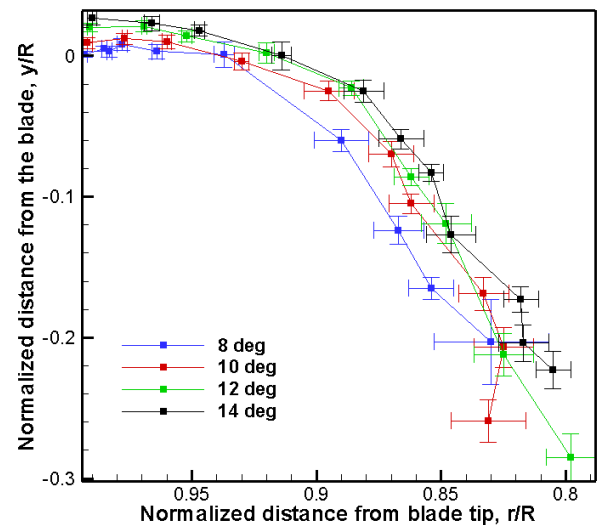


Figure 35. Vortex trajectory in PIV coordinates (uncorrected for blade coning and flap bending).

as observed in Fig. 36, is expected based on previous studies. The tip vortices moved above the blade ($y/R > 0$) before moving down.

At the early wake ages, radial contraction is significantly higher than after 90 degrees. When combining the radial and axial displacement observations, the tip vortices appear to stay in close proximity to the following blade. This is especially true for the 8-deg case, where the tip vortex at 90-deg wake age was directly impinging the following blade (see Fig. 17). The axial velocity increases with the collective pitch, as expected, because of the associated increase in the downwash velocity. A noticeable observation is the increased radial contraction with increasing collective.

Shadowgraphy data were acquired along the 0-180 degree azimuthal plane on both sides of the rotor. The 180-deg azimuth refers to the 80- by 120-ft wind tunnel inlet side and the 0-deg azimuth refers to the downstream (vane set 4) side of the shadowgraphy image (see Fig 2). When plotting the two resulting trajectories, axial trajectory was similar between the two sides. However, radial trajectory showed differences with the 0-deg azimuthal plane showing more contraction than the 180-deg azimuth (tunnel inlet) side. While the cause for such difference is yet unclear, PIV measured trajectories showed excellent correlation with the 0-deg azimuthal plane both in the axial direction as well as in the radial direction.

Comparing a hovering rotor wake to free-jet flow, while not a new idea, provides a perspective that can improve understanding of wake characteristics (Ref. 38, 39). Also, applying free-jet evolution knowledge to a rotor wake results in useful parameters to validate the wake measurements, as described next.

A jet boundary is the equivalent of the slipstream boundary (based on momentum theory) or the tip vortex path in a hovering rotor. Jet boundary is defined as the inflection point where (1) the slope of velocity near the edge of the jet reaches the

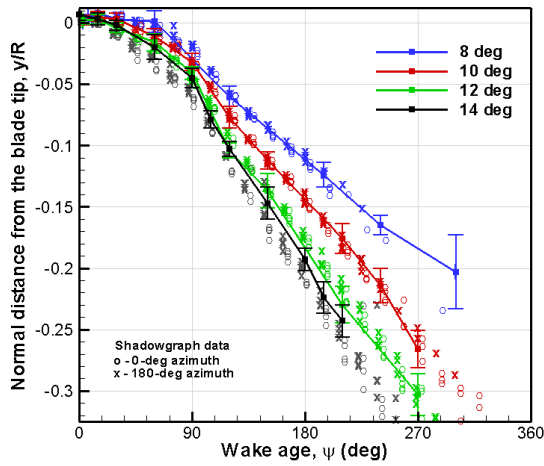


Figure 36. Comparison of tip vortex axial convection between PIV and shadowgraph data.

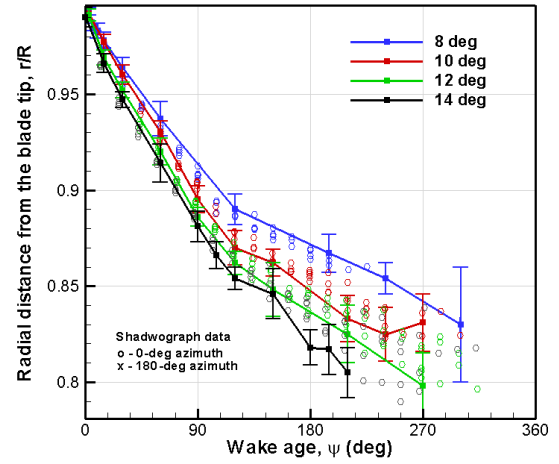
maximum, (2) the turbulence intensity is the maximum, or (3) the local velocity is half the peak velocity measured inside the jet. In a pure free-jet, all three will point to the same location. Assuming the rotor as a nozzle (rotor diameter = nozzle diameter), for each axial location (axial grid node), the radial location where the downwash velocity is half the maximum downwash velocity measured inboard is identified. The axial location spanned from the blade to one radius below the blade. Phase-averages obtained from the reduced sample set after applying vectorized projection are used for extracting free-jet boundaries from the rotor wake.

Figure 38 shows the tip vortex locations plotted against the identified jet boundary (using half-peak velocity) for all four collective pitch conditions. Excellent correlation is found between the jet boundary and the tip vortex locations. Tip vortices, in a hovering rotor wake, are expected to convect at half the downwash velocity because the tip vortices form the boundary separating quiescent flow on the outside and downwash on the inside (i.e., $\frac{0+v_i}{2}$). And, the jet boundary is identified as the location of half the downwash velocity. The benefit of relating a jet boundary to tip vortex locations can be seen in Fig. 38; long after tip vortices are indiscernible in the PIV measurement, wake contraction continued to occur until r/R reached 77%. Ideal wake contraction based on momentum theory is $\frac{1}{\sqrt{2}}$ or 0.707.

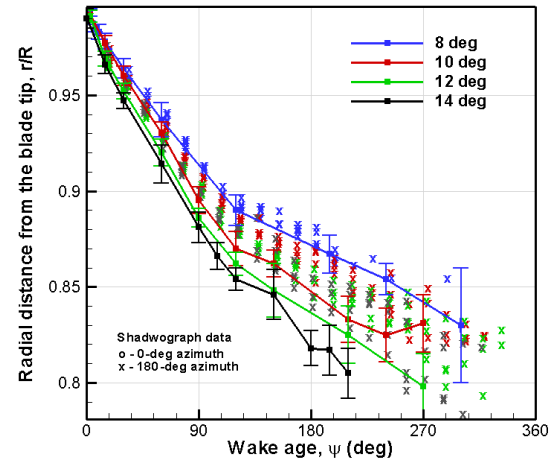
The hover induced velocity can be related to blade loading through

$$\frac{v_i}{\Omega R} = \sqrt{\frac{C_T}{2}} \quad (5)$$

using momentum theory. The flow accelerates with wake contraction until *vena contracta*, where the downwash velocity is twice the hover induced velocity. Applying Eq. 5 to the four test cases $CT/\sigma=0.057$ (8-deg), 0.077 (10-deg), 0.097 (12-deg), and 0.117 (14-deg), the maximum estimated downwash velocities are 21.2, 24.6, 27.6, and 30.3 m/s, respectively. Figure 39 shows the downwash velocity at $y/R=1$ for the four thrust conditions used in this experiment; excellent correlation is shown between the measured and the momentum the-



(a) At $\psi = 0^\circ$



(b) At $\psi = 180^\circ$

Figure 37. Comparison of radial contraction between PIV and shadowgraph data.

ory based downwash velocities.

Measured core radius and peak swirl velocity determined from the polar plots for all four collective pitch cases are shown in Fig. 40. The core radius generally increases with wake age because of viscous diffusion. Core growth trend is particularly clear for the 8- and 12-deg cases. For both 10- and 12-deg, as mentioned earlier, all the values are not determined for the same blade, i.e., every 90-deg wake age belongs to a different blade. So, drawing a conclusion from the measurement is difficult. To allow such analysis, a limited comparison among blades is discussed in Appendix C.

Unlike core radius, peak swirl velocity shows a clear trend for all four collective pitch conditions. As expected, at any given wake age, peak swirl velocity magnitude increases with collective pitch angles. The ratio of peak swirl velocity to tip speed of the rotor increased from 18% (for 8-deg case) to about 30% (for 14-deg case). All four collective pitch con-

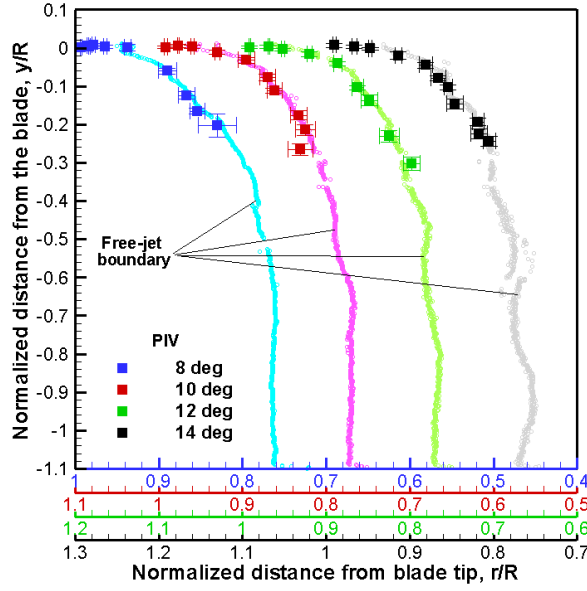


Figure 38. Wake slip stream boundary from free-jet calculations.

ditions show decreasing magnitude with increasing wake age. Such a trend is expected based on viscous diffusion that transfers the momentum from inside to outside of the vortex core.

Determining vortex circulation for an isolated vortex is straightforward. Circulation increases as radial distance from the vortex center increases. The rate of increase reduces outside the core boundary; however, the absolute magnitude continues to increase. Typically, vortex size is defined as the radius when the circulation is 99% of the vortex circulation (to allow for asymptotic increase). For an isolated vortex, the threshold is reached at 2-4 core radii and any further increase in circulation is asymptotical. Core circulation, which is simply the magnitude of circulation at the core radius, should not be confused with vortex circulation. Existing vortex models such as the laminar Lamb-Oseen or turbulent Iversen differ in the ratio of core circulation to vortex circulation. The ratios are about 70% and 50% for Lamb and Iversen models, respectively.

The problem with measuring the vortex circulation for a lifting wing/rotor lies in determining the size of the vortex (99% threshold). According to the Betz roll up theory, the vortex size can be on the order of the semispan of a wing or the radius of the rotor blade.

$$\Gamma_v(r_v) = \Gamma_b(r) \quad r_v = -\frac{1}{\Gamma_b(r)} \int_0^r \Gamma_b(r) dr \quad (6)$$

As the vorticity area integral or circular line integral is often used to determine circulation, Betz's theory introduces challenges because of the presence of the vortex sheet. An area as large as the rotor radius will include vorticity contained within the vortex sheet. So, an assumption is generally made to estimate vortex circulation. For example, Wolf et al. (Ref. 22) assumes the circulation measured at $0.5c$ from the vortex center as the vortex circulation. In the present study, curve-fit results

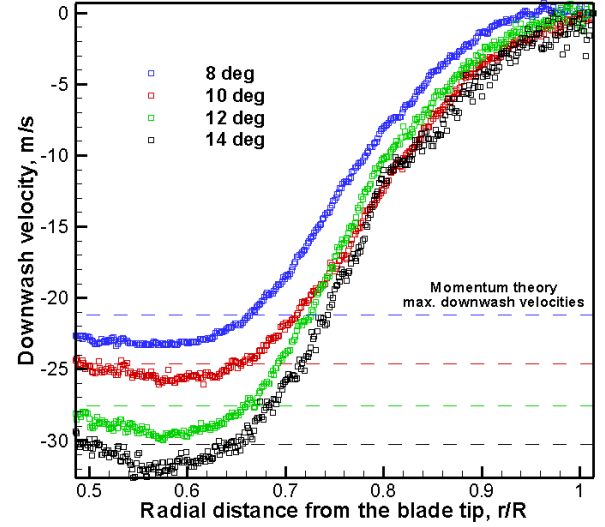


Figure 39. Downwash velocity variation. The dashed lines correspond to the maximum downwash velocity determined using momentum theory.

Table 2. Comparing circulation based blade loading to the measured values.

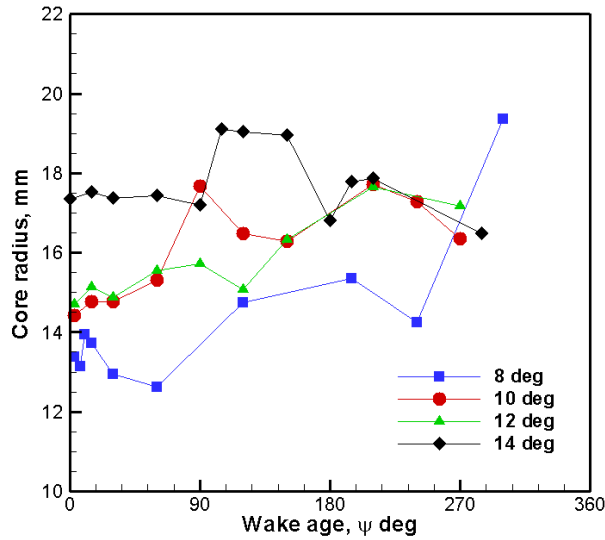
θ_0 (deg)	Γ_v m^2/s	C_T/σ From PIV (ideal)	C_T/σ Balance	Δ %
8	4.15	0.067	0.057	14.9
10	5.23	0.085	0.077	11.0
12	6.53	0.1057	0.097	8.9
14	7.93	0.128	0.117	9.4

are used. The advantage of using a curve-fit model to PIV flow field is that the resulting vortex characteristics are representative of the measured data. Calculating total vortex circulation allows conducting fundamental aerodynamic analysis on rotor wake. For example, blade loading can be estimated from tip vortex circulation with certain assumptions.

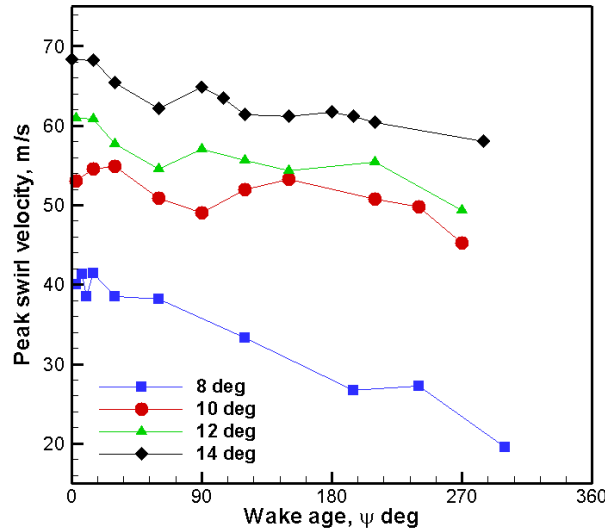
$$\frac{\Gamma_v}{\Omega R c} = k \frac{C_T}{\sigma} \quad (7)$$

The above equation assumes uniform distribution of circulation (ideal twist) and that the entire trailed vorticity occurs at the tip in the form of a tip vortex. In hover, $k = 2$. Results from substituting the vortex circulation (Γ_v) values for the four test conditions are compared against the measured blade loading in Table 2. There is a consistent over-prediction of blade loading values derived from PIV when compared to rotor balance measurements. The biggest difference is 15% for the 8-deg case that gradually reduces to 9% until the 12-deg case before increasing slightly to 9.4% for the 14-deg case.

In general, vortex circulation increases with blade collective pitch as expected. There are two common observations among the test cases when comparing vortex circulation (Fig. 41): (1) vortex circulation increases with wake age at early ages ($\zeta < 60^\circ$), and (2) there is a noticeable reduction in circulation



(a) Core size



(b) Peak swirl velocity

Figure 40. Measured vortex properties at various wake ages for various collective angles.

at the first blade passage (90°). Reduction in vortex circulation is often attributed to dissipation through energy cascading. However, the rate of reduction suggests other factors play a role.

The overpredicted vortex circulation (from the curve-fit results) and the marked reduction in magnitude at the first blade passage has a common source: tip vortex and returning wake interaction. This interaction is essential to understanding the wake evolution and is discussed in the next section.

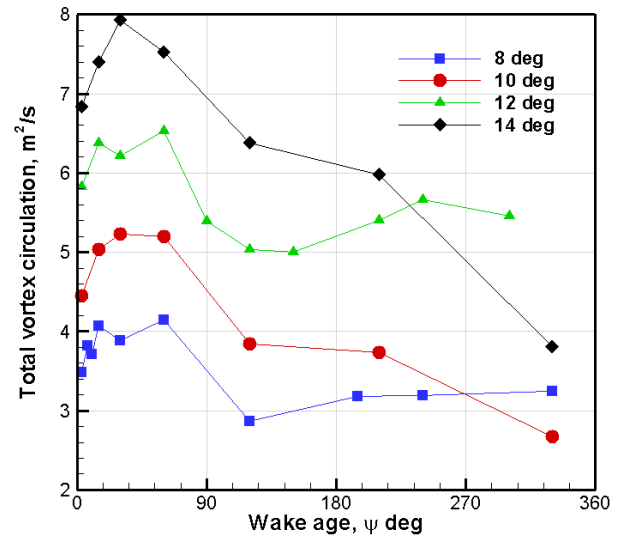


Figure 41. Total vortex circulation using curve-fit results. Trailed Circulation and Returning Wake

A circular line integral was applied from the tip of the blade to the measurement boundary (on the inboard section) after dividing the entire length surrounding the vortex and vortex sheet into several small rectangular regions within the dotted area marked in the PIV image insert in Fig. 42. The width (in the radial direction of the rotor blade) of each region was as small as three measurement nodes and the height (in the y-direction) was varied to maximize the spanwise length (restricted by blade shadow) as far inboard as possible. The resulting circulation from each region, which represents the trailed circulation, is plotted in Fig. 42.

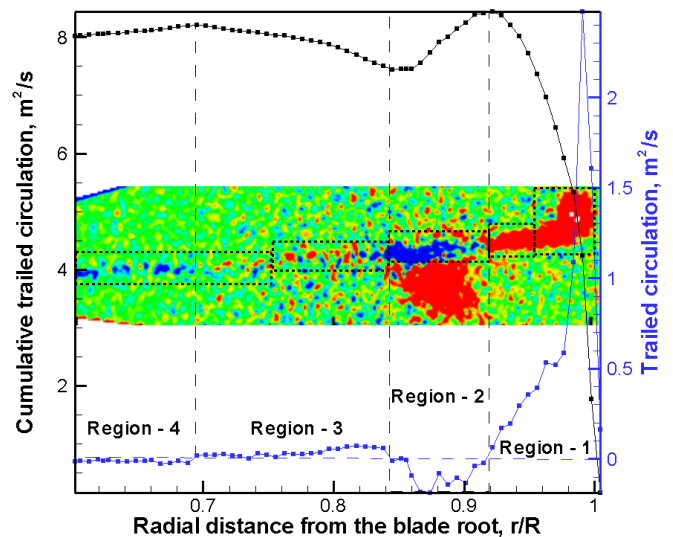


Figure 42. Trailed wake circulation and cumulative trailed wake circulation.

To conserve circulation, the strength of the trailed circulation at each radial station must be equal to the radial gradient of the bound circulation, i.e., $\Gamma_{tr} = \frac{d\Gamma_b}{dr}$. The fact that the bound circulation is zero at the tip (no lift) makes it possible to calculate

the sectional bound circulation from the blade tip. Starting from the blade tip and moving inboard, the sectional bound circulation can be determined by cumulatively adding trailed circulation (also shown in Fig. 42). The above procedure to calculate the magnitude of sectional bound circulation satisfies conservation requirements; however, the spanwise location of the trailed vortices (and circulation) still needs to be evaluated. The procedure is discussed next.

From Fig. 42, moving inboard, trailed circulation is positive in Region 1, followed by a small region of negative circulation (Region 2). Regions 1 and 2, therefore, produce increasing and decreasing cumulative trailed circulation magnitudes, respectively. In other words, the slope $d\Gamma_b/dr$ changes sign between the two regions. The trailed circulation in Region 3 is positive before turning slightly negative inboard (Region 4). The local sectional bound circulation (cumulative trailed circulation) reaches a local maximum value at $r/R=0.7$. Whenever the sign for the trailed circulation changes, a corresponding change in the slope $d\Gamma_b/dr$ is expected. Even though relating the trailed and sectional bound circulations should only be made after applying the inverse Betz method, Fig. 42 was used to enable understanding of the physics.

PIV measurements for the corresponding case is embedded for improved visualization in Fig. 42. All regions of positive trailed circulation show positive vorticity (red); regions of negative trailed circulation correspond to negative vorticity (blue).

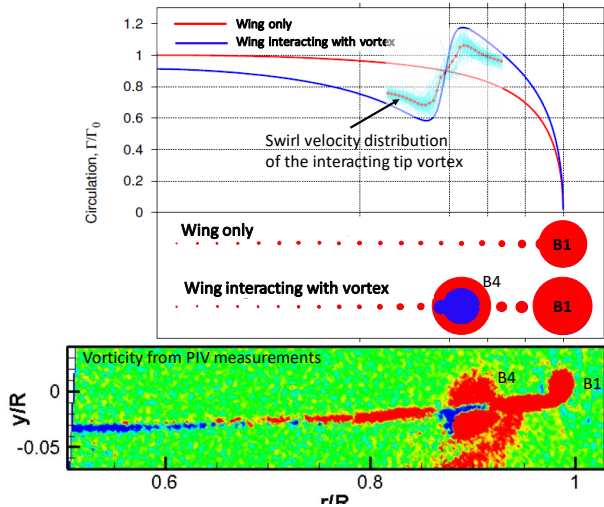


Figure 43. Increase in tip vortex strength caused by vortex interaction. Schematic was modified from Ref. 40 to match the color contours and configuration of the present measurements.

An interacting tip vortex induces upwash outboard and downwash inboard of the interacting spanwise location. An upwash increases the angle of attack (reducing the rotor inflow velocity) resulting in higher lift than without any interaction. Similarly, the induced downwash inboard adds to the rotor downwash resulting in reduced the angle of attack and reduced lift. The size of the region influenced by the interacting

vortex corresponds to the width of the negative trailed circulation in Fig. 42 or the width of the reduced sectional bound circulation. The reason for negative vorticity (and therefore negative trailed circulation) is the interaction of the tip vortex from blade 4 (previous blade). The center of the interacting vortex corresponds to the center of the bound circulation negative slope in Region 2. The increase in lift outboard of the blade 4 vortex interaction location directly affects the strength of the oncoming blade tip vortex (blade 1).

Figure 43 is a modified version of an image taken from the fixed-wing and wake interaction study (Ref. 40). The modification is done to match the color contours and orientation of the present measurements. Lifting-line calculations performed on a fixed-wing with and without vortex interaction (shown in Fig. 43) explains the increased vortex circulation. Tip vortices roll up all the vorticity (trailed circulation) from the blade tip until the spanwise location where the local peak circulation occurs. The increase in lift (and circulation) near the blade tip resulting from the blade 4 vortex interaction results in increased strength for the blade 1 vortex. In the absence of a vortex interaction, the tip vortex strength will be lower.

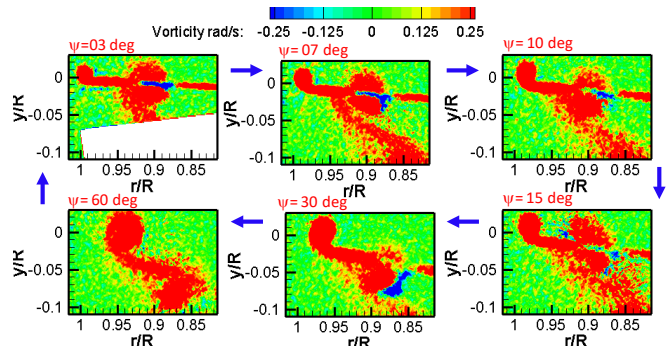


Figure 44. Wake evolution and the engulfing of negative circulation by blade 4 vortex.

Higher circulation of the tip vortex directly translates to higher blade loading based on Eq. 7. While Eq. 7 expects uniform circulation, the increased circulation near the tip caused by the blade 4 vortex interaction (when combined with Betz roll-up theory) explains the higher blade loading derived from the PIV measurements in Table 2.

The differences between PIV-based and rotor-balance-based blade loadings (shown in Table 2) for varying collective pitch conditions (15% at 8 deg and 9.4% at 14 deg) is a result of the vertical separation (“miss distance”) between the blade 1 vortex sheet and the interacting blade 4 vortex. At 8 deg, the interaction is direct (as shown in Fig. 17). As collective pitch increases, the associated downwash pushes the blade 4 vortex downward, thereby increasing the miss distance. A smaller miss distance produces higher outboard circulation that, in turn, increases the deviation from the ideal, uniform circulation assumed in Eq. 7. A larger miss-distance, on the other hand, brings the vortex circulation and blade loading closer to the ideal values, explaining the varying differences in PIV

based blade loading and the balance based blade loading seen in Table 2.

To continue with the vortex interaction analysis, the negative trailed circulation inboard of the interaction is absorbed by the blade 4 vortex over time. Figure 44 shows the close-up view of such absorption for the 8-deg case, where the blade 4 vortex directly impinges on the vortex sheet. The blue color areas represent the negative vorticity caused by the interaction, which is rolled up into the blade 4 vortex as wake age increases. The addition of negative vorticity (and the associated negative circulation) to the blade 4 vortex circulation is the primary reason for the marked reduction in vortex circulation at the first blade passage observed in Fig. 41.

Inboard sections ($r/R < 0.7$) also show negative trailed circulation (negative vorticity in Fig. 43). As mentioned earlier, the negative vorticity is a result of bound circulation reaching the peak magnitude at 70% span that slowly reduces towards the root of the blade (where the lift is zero).

Airloads Distribution From PIV

One of the potential benefits of the PIV velocity measurements is the ability to reverse-calculate the blade loading distribution. One such calculation was previously demonstrated for the wake interaction with a fixed wing (Ref. 40). The process of Ref. 40 is extended and applied for the first time to rotor blades in the present effort. As mentioned earlier, the Betz roll-up theory forms the basis for the analysis.

The magnitude of sectional bound circulation calculated from PIV measurements reflects the trailed circulation distribution; however, the spatial locations of the trailed vorticity need to be calculated. According to Betz theory, as trailed vortices roll into a tip vortex, circulation measured at a given tip vortex radius can be directly related to the circulation trailing from a specific spanwise location in the rotor blade (as shown in Eq. 6). Rossow (Ref. 41) developed a procedure that reverses the Betz roll-up calculations by tracing back the circulation contained within the tip vortex and relating the circulation to the blade spanwise position. The inverse-Betz procedure is based on the circulation distribution of the tip vortex and the vortex sheet that spans across the blade, i.e.,

$$\Gamma_b(r) = \Gamma_v(r_v) \quad R - r = r_v + \int_0^{r_v} \frac{x}{\Gamma_v(x)} \frac{d\Gamma_v(x)}{dx} dx \quad (8)$$

Figure 45 compares the raw measurement of trailed circulation obtained from the PIV grids against the inverse Betz methodology. As expected, the trailed vortex locations are pushed inboard “unwinding” the circulation layers from the tip vortex. With both magnitude and the spatial locations identified, the next step is to relate the calculations to loading distribution ($M(r)^2 c_n$) on the blade. Kutta-Joukowski theorem relates lift per unit span of the rotor blade to the trailed circulation using

$$dL = \rho(\Omega r)\Gamma(r)dr = \frac{1}{2}\rho(\Omega r)^2 c(r) c_l(r) dr \quad (9)$$

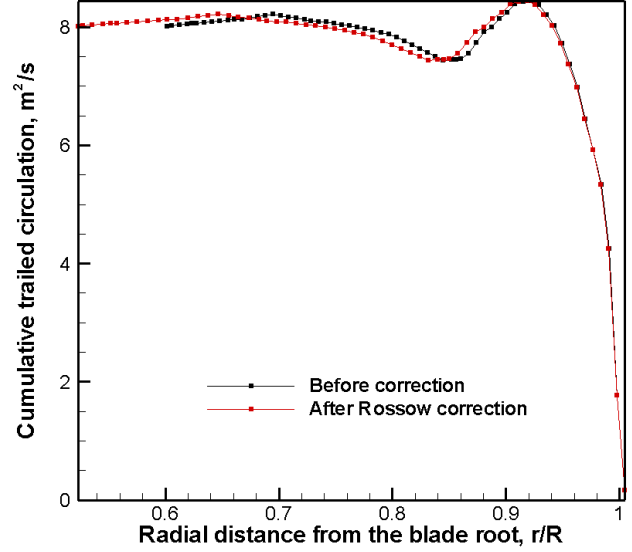


Figure 45. Locating the radial position of trailed circulation from wake circulation using Rossow correction.

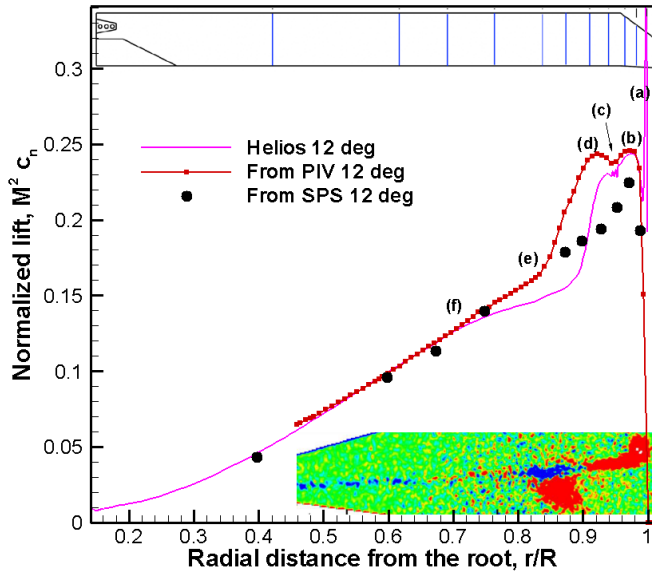
Simplifying the above equation results in

$$c_l(r) = \frac{2 \Gamma(r)}{\Omega r c(r)} \quad (10)$$

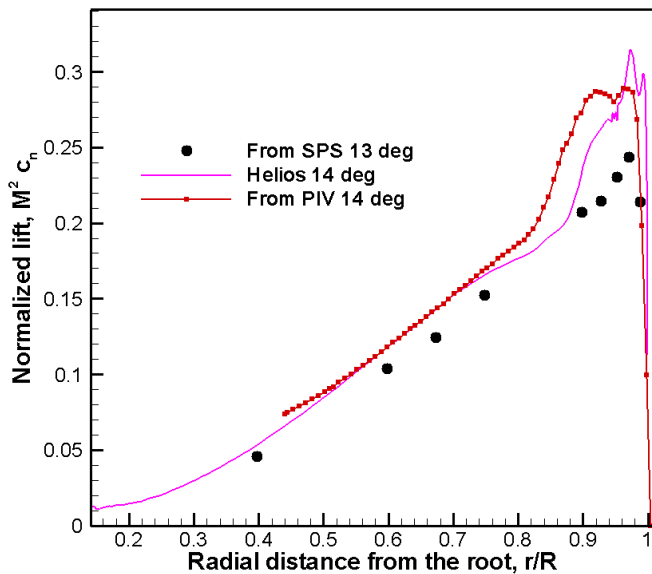
Sectional loads calculated using the above equation after substituting the measured $\Gamma(r)$ from the PIV flow field for the 12-, and 14-deg cases are shown in Fig. 46. For the 8- and 10-deg cases, the blade 1 vortex sheet and blade 4 vortex were very close in proximity; separating trailed circulation from the vortex sheet was not practical without the application of a vortex model. For the 12 deg case, an artificially stretched PIV image that mimics the inverse roll up proposed by Rossow along with a schematic for the blade (for chord distribution) are also added to Fig. 46 for easier analysis. The HVAB blade has a reduced chord from 95% spanwise location to the tip. Simulations from Helios (Ref. 4) are also included. The figure is annotated with letters marking important locations for discussion.

All three methods show an initial increase in normalized lift near the blade tip. Helios, with the necessary spatial resolution, shows a sharp increase (a) caused by the tip vortex upwash. Moving inboard, airloads determined from integrating surface pressures (from surface pressure sensors or SPS) and PIV (trailed wake) show peak values (b). Helios shows a second local peak at the same spanwise location, as well. While Helios and PIV airloads agreed in peak magnitude, both are higher than the SPS values.

From the peak location, SPS based airloads reduced almost linearly towards inboard sections. However, both PIV and Helios showed an additional peak (d) that correspond to where the positive vorticity (or positive trailed circulation) ends and negative trailed circulation starts. Between (b) and (d), there was a small reduction in lift at (c) that aligned with the 95%



(a) 12 deg



(b) 13/14 deg

Figure 46. Comparison of airloads among between two experimental methods (PIV and surface pressure) and Helios.

span location. The region between *(d)* and *(e)* relates to the negative trailed circulation resulting in a marked decrease in lift. Even though both the Helios and PIV measurements showed the lift reduction, the spatial location and the width of such reduction are different. The difference in the spatial location of segment *(b) – (d)* results from the difference in the radial location of the returning wake vortex B4 between the two techniques (Ref. 4). The B4 vortex was located at $r/R = 0.87$ and 0.90 for PIV and Helios, respectively. Consequently, a larger section of vortex sheet (positive) between the

B1 and B4 tip vortices adds to the higher cumulative circulation (and, therefore, higher lift at *(d)*) for PIV when compared to Helios.

Between *(e)* and *(f)*, positive trailed circulation counteracts the effect of reducing local Mach number, thereby shallowing the slope of the reducing lift. At *(e)* Helios and PIV differ because of the difference in the spanwise distribution of negative trailed vorticity. The magnitudes are, otherwise, the same. Ultimately, from inboard of *(f)*, effect of local Mach number dictates the normalized lift reduction and all three methods show similar magnitude and trend.

Figure 46b shows similar results for the 14-deg case. For SPS based measurements, the collective pitch was 13 degrees. Consequently, no direct comparison of peak magnitude at *(a)* can be assessed. Nevertheless, all the features explained for the 12-deg case exist for the 14-deg case. For example, the peak magnitudes, and all the regions from the first local PIV lift peak near the tip at *(b)* to the inboard region are similar between Helios and PIV. Also, the difference between Helios and PIV in terms of the spanwise location and width that covers negative trailed circulation continues to exist.

Airloads from the SPS measurements are derived from distributed pressure sensors along the chord by integration at every span location. Helios predictions are based on a high number of surface grid nodes at a given chord and along the span. PIV-based airloads derived from the wake measurements essentially includes and integrates all the aerodynamic and aeroelastic effects occurring on the blade. In other words, Helios values along the chord are integrated mathematically, PIV values are inherently integrated aerodynamically. Consequently, PIV-based airloads and Helios show good correlation with each other, especially the double-lobe pattern at *(b)* and *(d)* probably because of the higher resolution.

The added circulation peak at *(d)* in the case of PIV and Helios is not present in the SPS measurement. More SPS sensors are needed both along the chord and the span to capture all the features, which is impractical for a rotor blade of this size. While drawing conclusions from the aforementioned comparisons on airloads distribution, it should be remembered that the integrated loads from the rotor balance, i.e., blade loading (while agreeing with Helios) differ from Kutta-Joukowski theorem based PIV blade loading when ideal inflow distribution is assumed. So, care must be taken when inferring integrated blade loading (C_T/σ) from PIV when vortex interaction is involved. Nevertheless, PIV-based airloads distribution ($M^2 c_n$) appear to provide a second approach for small rotors, where surface pressure sensors cannot be embedded.

CONCLUSIONS

Wake measurements on a hovering rotor using stereoscopic PIV was successfully conducted in the NFAC 80- by 120-ft wind tunnel test section. Acquiring high fidelity data for simulation validation was the primary objective of the HVAB test campaign. Standard rotor wake data that includes wake trajectory, tip vortex core size, strength, and their evolution were measured and added to the HVAB data set.

To ensure consistency of the high quality results, substantial effort was undertaken. The presented work focused on three key aspects in analyzing data: (1) reducing uncertainty, (2) comparing with other measurements made during the HVAB test campaign and aerodynamic theories, and (3) developing a methodology to extract airloads from the PIV velocity field. The analysis revealed the HVAB dataset is self-consistent. Following are the specific conclusions derived from the study in each of those aspects.

1. Two novel data analysis methodologies to remove outlier realizations were developed: (1) Modal outlier method (MOM), and (2) Projection on Phase-average (POP). Removing realizations affected by poor density smoke was the goal. MOM is useful when the outlier count is minimal and the signal to noise ratio is high. POP is applicable when the data has a high number of outliers. The two different methodologies were cross-validated with each other.
2. Upon successfully removing the outliers, the overall standard deviation was reduced substantially (some times as high as 70%). The effect of removing outliers also had a profound effect on the mean velocities as well. Accurately quantifying standard deviation and mean are required for accurate determination of turbulent intensity in the flow field that affects the wake evolution.
3. Aperiodicity inherent to rotor tip vortices was accounted for before calculating the statistics. Tip vortex properties were measured around the vortex (not through horizontal or vertical cuts) following the best practices developed over the years. Furthermore, a data acceptance criterion comparing vortex circulation obtained from circular line integral with a Lamb model based curve fit results was developed and applied. Accepted data were further validated against vectorized projection results.
4. Treating the lifting rotor as a free-jet, the tip vortex trajectory was compared against the free-jet boundary. Excellent correlation was found, allowing the rotor wake boundary to be traced after the tip vortices became indiscernible in the PIV measurements. A wake contraction ratio of 0.77 was obtained from the tip vortex locations and free-jet boundary.
5. Excellent correlation in tip vortex trajectory was found between PIV and the shadowgraphy data acquired at 0-deg azimuth. Shadowgraphy data acquired at 180-deg azimuth was slightly different from the 0-deg azimuth in the radial contraction. The cause of such deviation is still under analysis.
6. Early wake age tip vortex locations validated blade coning and flap bending deflections measured using photogrammetry. Also, measured downwash velocities matched the momentum theory estimations accurately for all collective pitch conditions, adding confidence to the consistency of the dataset.

7. Blade airloads distribution derived from the trailed wake (PIV) matched the overall trend exhibited by both the conventional surface pressure sensor (SPS) based airloads and the computational simulation (Helios). Trailed wake circulation was determined by applying a circular line integral to the tip vortex and vortex sheet trailing behind the rotor blade. Finer details in the loads distribution determined from PIV augment the airloads measured from SPS.
8. Combining PIV, inverse Betz theory, lifting line calculations, and Helios allowed analyzing the role of vortex interaction on the overall HVAB wake evolution. When the miss-distance (between the preceding blade vortex and the oncoming blade) is small, circulation strength of the new vortex is higher than when the miss distance is larger. Similarly, after the interaction, vortex circulation reduces markedly because of the rollup of negative vorticity into the interacting vortex.

ACKNOWLEDGMENTS

The authors gratefully acknowledge the significant efforts of the project partners (NASA, U.S. Army) as well as the U.S. Air Force, in the planning, preparation, and execution of this test, particularly Susan Gorton (NASA) and Oliver Wong (U.S. Army) for the decade-long support and advocacy for this entire research effort. The U.S. Air Force team, led by Paul Gilles for the PIV portion of the HVAB test, is gratefully acknowledged for running the test smoothly. The efforts of DLR Gottingen consultants (Markus Raffel and Christian Wolf, through the NASA-DLR MoU Arrangement for Experimental Optical Methods Applied to Rotorcraft) deserve special recognition for their key contributions to the success of this program. The authors would like to thank Dr. Mahendra Bhagwat (S&T, U.S. Army) for discussions related to aerodynamic analysis of wing-wake interaction and tip vortex modeling. The authors acknowledge the insightful discussions with Drs. Chris Cameron and David Schatzman on data analysis. The efforts of Mr. Rohit Jain (U.S. Army) for providing Helios simulation results related to the test for comparison and analysis are appreciated. Finally, special recognition is given to the late Frank Caradonna for his original design of the ARTS and the vision of a benchmark hover test.

REFERENCES

1. Johnson, W., "Wake Model for Helicopter Rotors in High Speed Flight," NASA CR-1177507, USAVSCOM TR-88-A-008, November 1988.
2. Johnson, W., "Rotorcraft Aerodynamics Models for a Comprehensive Analysis," American Helicopter Society 54th Annual National Forum, Washington, D. C., May 20-22 1998.
3. Bhagwat, M. J., and Leishman, J. G., "Generalized Viscous Vortex Core Models for Application to Free-Vortex

- Wake and Aeroacoustic Calculations,” American Helicopter Society 58th Annual Forum, Montréal, Canada, June 11–13 2002.
4. Jain, R., “CFD-CSD Pre-test Hover Predictions Validation for the HVAB Rotor” AIAA 2024-0893, AIAA SciTech 2024 Forum, Orlando, FL, 8–12 January, 2024, <https://doi.org/10.2514/6.2024-0893>
 5. Drees, J. M., and Hendal, W. P., “The Field of Flow Through a Helicopter Rotor Obtained from Wind Tunnel Smoke Tests,” *Journal of Aircraft Engineering*, Vol. 23, (266), February 1950, pp. 107–111.
 6. Landgrebe, A. J., “An Analytical Method for Predicting Rotor Wake Geometry,” AIAA/AHS VTOL Research, Design & Operations Meeting, Atlanta, GA, February 1969.
 7. Cook, C. V., “The Structure of the Rotor Blade Tip Vortex,” Paper 3, Aerodynamics of Rotary Wings, AGARD CP-111, September 13–15, 1972.
 8. Tung, C., Pucci, S. L., Caradonna, F. X., and Morse, H. A., “The Structure of Trailing Vortices Generated by Model Helicopter Rotor Blades,” NASA TM 81316, 1981.
 9. Egolf, T. A., and Landgrebe, A. J., “Helicopter Rotor Wake Geometry and its Influence in Forward Flight, Vol. 1 – Generalized Wake Geometry and Wake Effects in Rotor Airloads and Performance,” NASA CR-3726, October 1983.
 10. Leishman, J. G., and Bi, N., “Measurements of a Rotor Flowfield and the Effects on a Body in Forward Flight,” *Vertica*, Vol. 14, (3), 1990, pp. 401–415.
 11. Lorber, P. F., Stauter, R. C., Pollack, M. J., and Landgrebe, A. J., “A Comprehensive Hover Test of the Airloads and Airflow of an Extensively Instrumented Model Helicopter Rotor,” Vol. 1–5, USAAVSCOM TR-D-16 (A-E), October 1991.
 12. Bagai, A., Moedersheim, E., and Leishman, J. G., “Developments in the Visualization of Rotor Wakes using the Wide-Field Shadowgraph Method,” *Journal of Flow Visualization & Image Processing*, Vol. 1, (3), July–September 1993, pp. 211–233.
 13. McAlister, K. W., “Measurements in the Near Wake of a Hovering Rotor,” Proceedings of the 27th AIAA Fluid Dynamic Conference, New Orleans, LA June 18–20, 1996.
 14. Caradonna, F., Hendley, E., Silva, M., Huang, S., Komerath, N., Reddy, U., Mahalingam, R., Funk, R., Wong, O., Ames, R., Darden, L., Villareal, L., and Gregory, J., “An Experimental Study of a Rotor in Axial Flight,” AHS Technical Specialists’ Meeting for Rotorcraft Acoustics and Aerodynamics, Williamsburg, VA, October 28–30, 1997.
 15. Mahalingam, R., and Komerath, N. M., “Measurements of the Near Wake of a Rotor in Forward Flight,” AIAA Paper 98-0692, 36th Aerospace Sciences Meeting & Exhibit, Reno, NV, January 12–15, 1998.
 16. Leishman, J. G., Han, Y. O., and Coyne, A. J., “Measurements of the Velocity and Turbulence Structure of a Rotor Tip Vortex,” *AIAA Journal*, Vol. 35, (3), March 1997, pp. 477–485.
 17. Martin, P. B., Pugliese, G., and Leishman, J. G., “High Resolution Trailing Vortex Measurements in the Wake of a Hovering Rotor,” American Helicopter Society 57th Annual National Forum, Washington, DC, May 9–11, 2001.
 18. Norman, T. R., Heineck, J. T., Shairer, E. T., Schaeffler, N. W., Wagner, L. N., Yamauchi, G. K., Overmeyer, A. D., Ramasamy, M., Cameron, C. G., Dominguez, M., and Sheikman, A. L., “Fundamental Test of a Hovering Rotor: Comprehensive Measurements for CFD Validation,” The Vertical Flight Society 79th Annual Forum and Technology Display, West Palm Beach, FL, 16–18, May 2023.
 19. Martin, P. B. and Leishman, J. G., “Trailing Vortex Measurements in the Wake of a Hovering Rotor with Various Tip Shapes,” American Helicopter Society 58th Annual National Forum, Montréal Canada, July 11–13, 2002.
 20. Ramasamy, M., Leishman, J. G., and Lee, T. E., “Flow Field of a Rotating Wing MAV,” *Journal of Aircraft*, Vol. 44, (4), July 2007, pp. 1236–1244.
 21. Yamauchi, G., Wadcock, A., Johnson, W., and Ramasamy, M., “Wind Tunnel Measurements of Full-Scale UH-60A Rotor Tip Vortices,” American Helicopter Society 68th Annual Forum and Technology Display, Fort Worth, TX, May 13, 2012.
 22. Wolf, C. C., Braukmann, J., and Muller, M. M., “Tip Vortex Study of a Rotor with Double-Swept Blade Tips,” *AIAA Journal*, February 2024, DOI: 10.2514/1.J063426.
 23. Chaderjian, N. M. and Ahmad, J. U., “Navier-Stokes Assessment of Test Facility Effects on Hover Performance,” American Helicopter Society 71st Annual Forum and Technology Display, Virginia Beach, VA, 5–7 May 2015.
 24. Jain, R., “Effect of Facility Walls and Blade Aeroelasticity on PSP Rotor Hover Performance Predictions,” AIAA-2018-0305, AIAA SciTech 56th Aerospace Sciences Meeting, Kissimmee, FL, 8-12 January 2018. DOI: 10.2514/6.2018-0305
 25. <https://rotorcraft.arc.nasa.gov/HVAB/>
 26. Ghimire, H. C., Sean, C., and Bailey, C., “An Experimental Investigation of Wing-Tip Vortex Decay in Turbulence,” *Physics of Fluids*, Vol. 29, No. 3, March 2017, <https://doi.org/10.1063/1.4979133>.

27. Yoon, S., Chaderjian, N. M., Pulliam, T. H., and Holst, T. L., "Effect of Turbulence Modeling on Hovering Rotor Flows," 45th AIAA Fluid Dynamics Conference, Dallas, TX, 22–26 June 2015.
28. Sirovich, L., "Turbulence and the dynamics of coherent structures, Part 1: Coherent structures," *Quarterly Applied Mathematics*, Volume 45, No. 3, 1987, pp 561–571.
29. Leishman, J. G., "On the Aperiodicity of Helicopter Rotor Wakes," *Experiments in Fluids*, Vol. 25, 1998, pp. 352–361.
30. Heineck, J. T., Yamauchi, G. K., Wadcock, A. J., Lourenco, L., and Abrego, A. I., "Application of Three-Component PIV to a Hovering Rotor Wake," American Helicopter Society 56th Annual National Forum, Virginia Beach, VA, May 2–4, 2000.
31. Ramasamy, M., Johnson, B., Huisman, T., and Leishman, J. G., "A New Method for Estimating Turbulent Vortex Flow Properties from Stereoscopic DPIV Measurements," American Helicopter Society 63rd Annual National Forum, Virginia Beach, VA, May 1–3 2007.
32. van der Wall, B. G., and Richard, H., "Analysis Methodology for 3C-PIV Data of Rotary Wing Vortices," *Experiments in Fluids*, Vol. 40, 2006, pp. 798–812.
33. Ramasamy, M., Paetzel, R., and Bhagwat, M. J., "Aperiodicity Correction for Rotor Tip Vortex Measurements, American Helicopter Society 67th Annual Forum and Technology Display, Virginia Beach, VA, May 35, 2011.
34. Graftieaux, L., Michard, M., and Grosjean, N., "Combining PIV, POD and Vortex Identification Algorithms for the Study of Unsteady Turbulent Swirling Flows," *Measurement Science and Technology*, Vol. 12, Aug. 2001, pp. 1422–1429. DOI: 10.1088/0957-0233/12/9/307.
35. Mula, S. W., Stephenson, J. H., Tinney, C. E., and Sirohi, J., "Dynamical Characteristics of the Tip Vortex From A Four-Bladed Rotor in Hover," *Experiments in Fluids*, Vol. 54, 1600, No. Oct. 2013, <https://doi.org/10.1007/s00348-013-1600-9>.
36. Lamb, H., *Hydrodynamics*, 6th ed., Cambridge University Press, Cambridge, 1932, pp. 592–593.
37. Iversen, J. D., "Correlation of Turbulent Trailing Vortex Decay Data," *Journal of Aircraft*, Vol. 13, No. 5, May 1976, pp. 338–342.
38. Spalart, P. R., "On the Flow Field Induced by a Hovering Rotor or a Static Jet," *Journal of Fluid Mechanics*, Vol. 701, May 2012, pp. 473–481.
39. Ramasamy, M., Yamauchi, G. K., and Potsdam, M., "Measurements to Understand The Flow Mechanisms Contributing To Tandem-Rotor Outwash," American Helicopter Society 71st Annual National Forum, Virginia Beach, Va., May 2015.
40. Bhagwat, M. J., Ramasamy, M. J., and Caradonna, F. X., "Fundamental Characterization of Spanwise Loading and Trailing Wake Vortices," American Helicopter Society 71st Annual National Forum, Virginia Beach, Va., May 2015.
41. Rossow, V. J., "Prediction of Span Loading from Measured Wake-Vortex Structure -An Inverse Betz Method," *Journal of Aircraft*, Vol. 12, No. 7, July 1975, pp. 626–628, <https://doi.org/10.2514/3.59845>.

APPENDIX A

Simple phase-averaged vector fields for selected cases at various wake ages for 8-deg collective pitch condition are shown in Fig. A1 and A2. Both vorticity contours and out-of-plane streamwise velocity (excess) are plotted. The vorticity contours track the location of tip vortices as well the vortex sheet. The change in sign of the vorticity in the vortex sheet along the span where the maximum circulation occurs can be observed as well. The streamwise velocity excess better captures the vortex sheet than the vorticity contour over a longer period of time (about 7 blade passages). Similar observations were made for the 10 to 14 deg cases (not shown). The number of vortex sheets visible within the PIV measurement region reduces gradually with higher collective pitch because of higher downwash velocities associated with higher thrust conditions.

APPENDIX B

Figures B1 and B2 show the application of acceptance criterion for the relatively noisy, 12-deg collective pitch case that resulted in only 35 out of 200 samples meeting the criterion. Considering the high rejection number, the *selected* (rather than the rejected) samples are marked with a black square box for clarity. Figure B2 shows, similar to the 8-deg case, that the majority of the selected samples are those with high vectorized projection sum (with a few exceptions). Figures B3 through B6 show the following results in order: horizontal and vertical cuts of swirl velocity profiles, mean profiles that include circulation, and the polar plots of core size and peak swirl velocity distributions. Though alarming to see that the horizontal/vertical cuts show few data points near the vortex center, the scarcity of points do not play a role in determining core size or peak swirl velocity. Lack of points at the center is still preferred over interpolated values that do not add value. So, despite a small sample set, using the velocity values around the vortex were confidently used to determine the core size and peak swirl velocity.

For the 12-deg case, the mean core radius and peak swirl velocity measured around the vortex are 16.32 mm and 54.29 m/s, respectively. The standard deviations are about 1.10 mm and 6.33 m/s, respectively.

APPENDIX C

Fig C1 shows the vortex trajectories at 8-deg collective for both blade 1 and 3. The opposing blades in a four-bladed system were selected for comparison to understand the trajectory

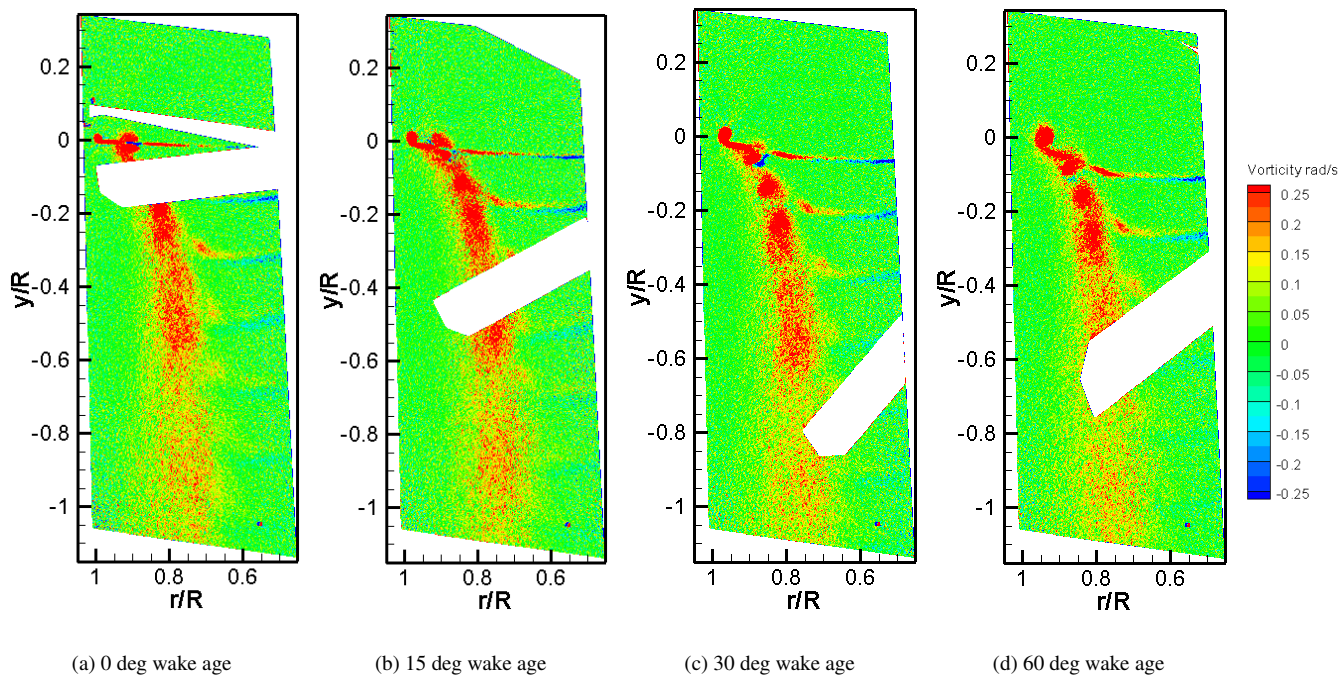


Figure A1. Collective pitch: 8 deg - vorticity.

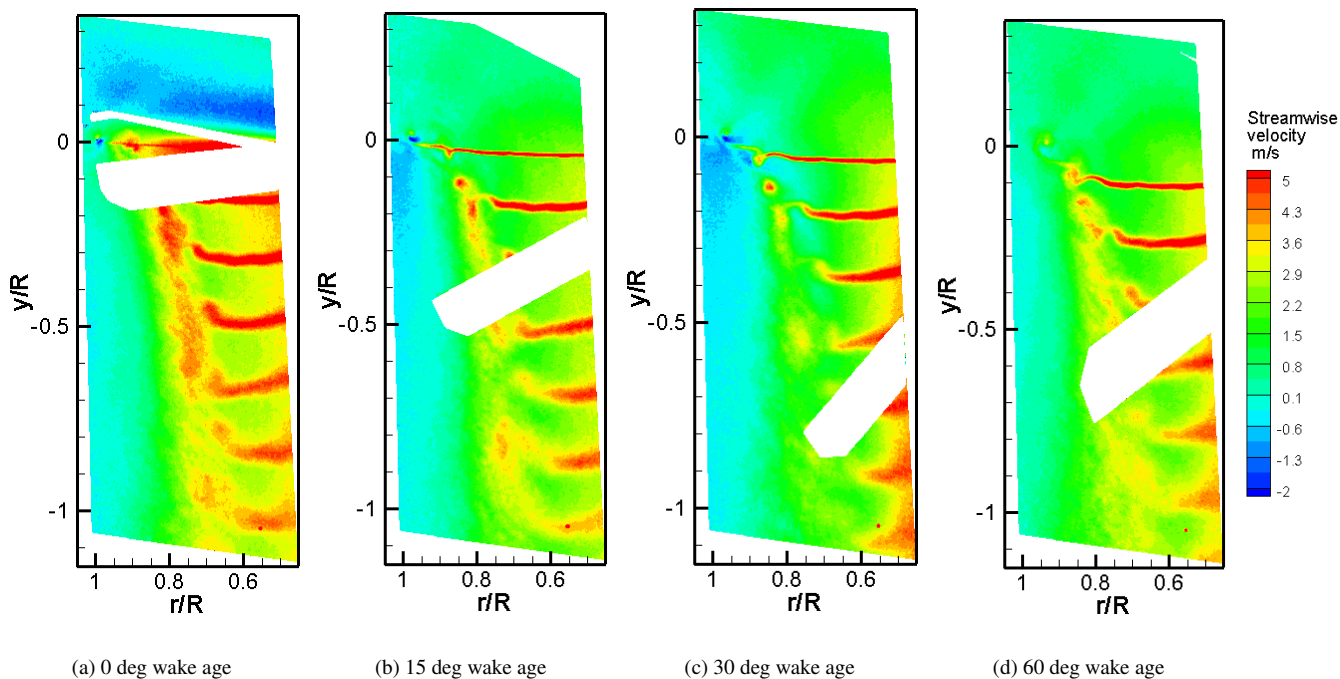


Figure A2. Collective pitch: 8 deg - streamwsie velocity.

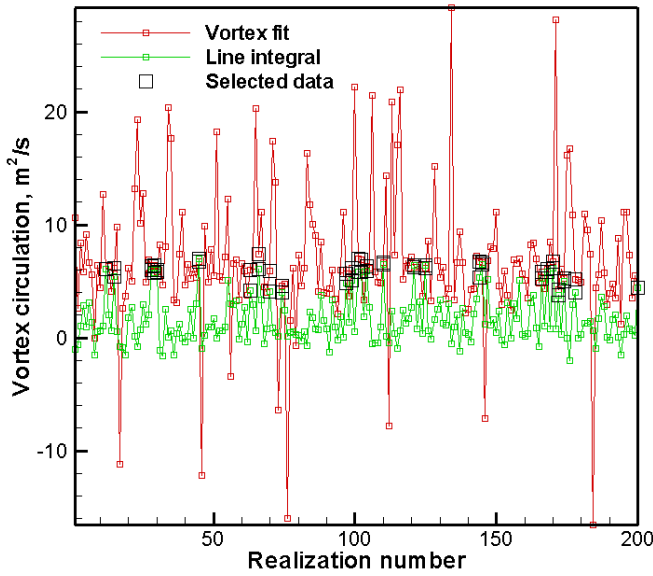


Figure B1. Comparison of vortex circulation determined using vortex fit method and line integral ($\psi = 150^\circ$).

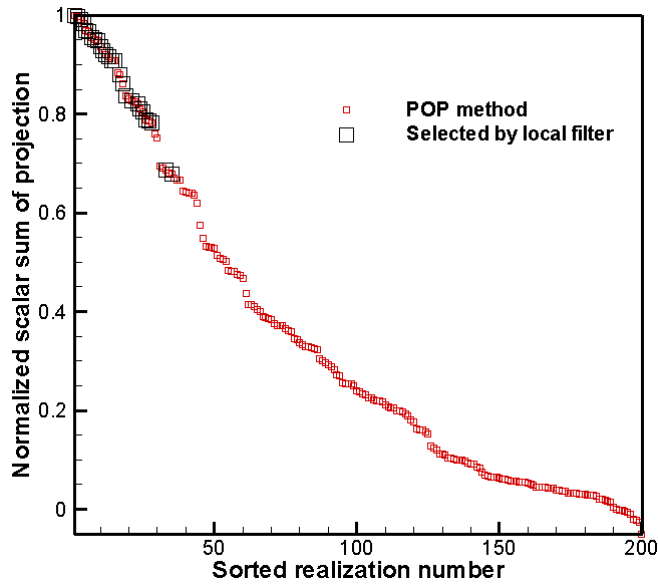
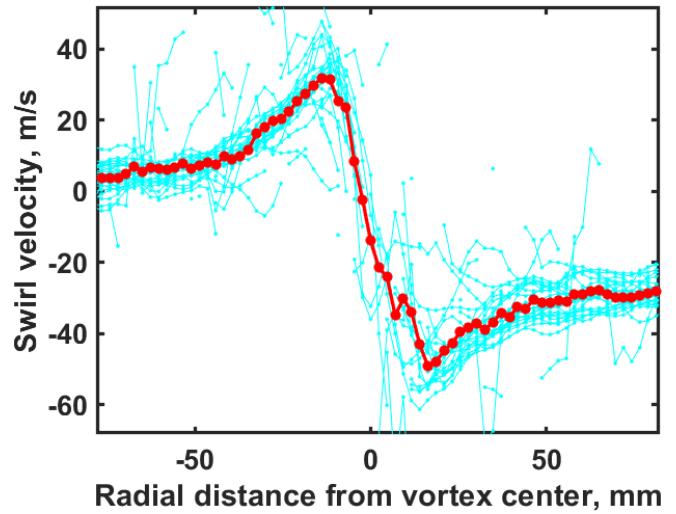


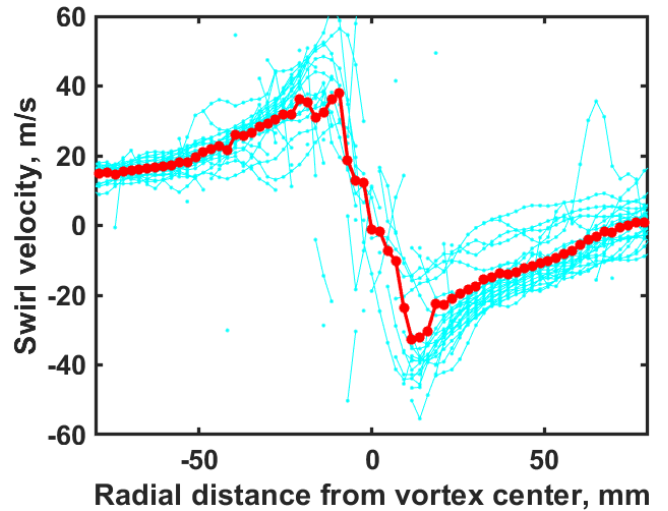
Figure B2. Realizations showing the relative rank of selected data.

differences observed in the Shadowgraphy data (Ref. 18). A 2nd-order polynomial curve-fit allowed visualizing the difference observed between the two blades. The blade 3 wake appears to contract more than Blade 1 at older wake ages. Scatter is lower at early wake ages and, as expected, gradually increases with time. The scatter is also more in the radial direction than the axial direction for both blades. In terms of absolute magnitude, the scatter is the same for both the blades except at the oldest measured wake age for Blade 1.

The core size and peak swirl velocities are plotted in Fig. C2. The measurements show the same trend with increasing core size and decreasing peak swirl velocity magnitude with wake age. No significant difference is noticed between the blades.

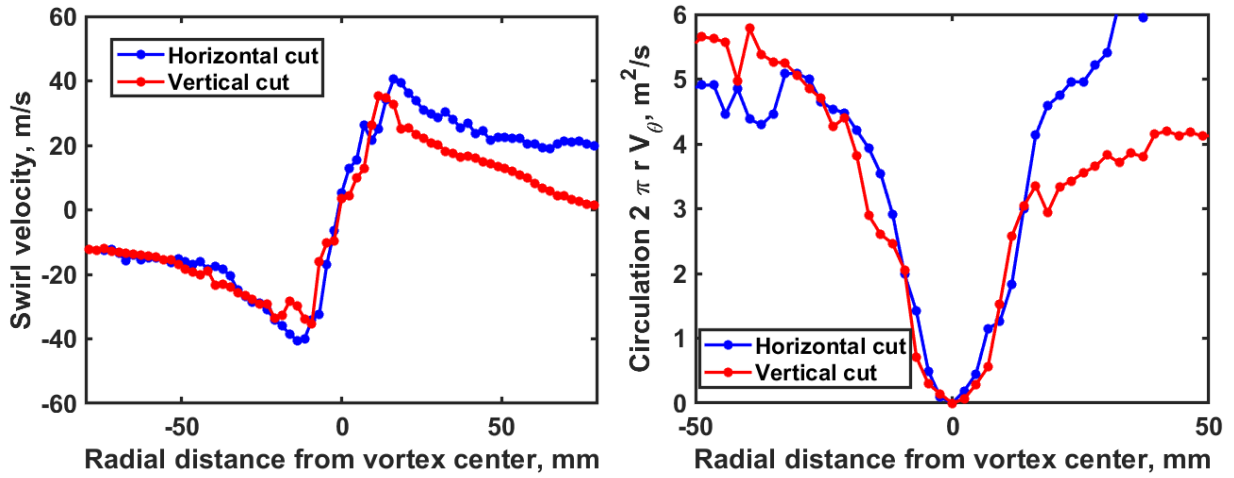


(a) Horizontal cut



(b) Vertical cut

Figure B3. Horizontal and vertical cuts through the center.



(a) Centered mean swirl velocity profiles

(b) Circulation

Figure B4. Swirl velocity and circulation distribution mean - $\theta_0 = 12^\circ$, $\psi = 150^\circ$.

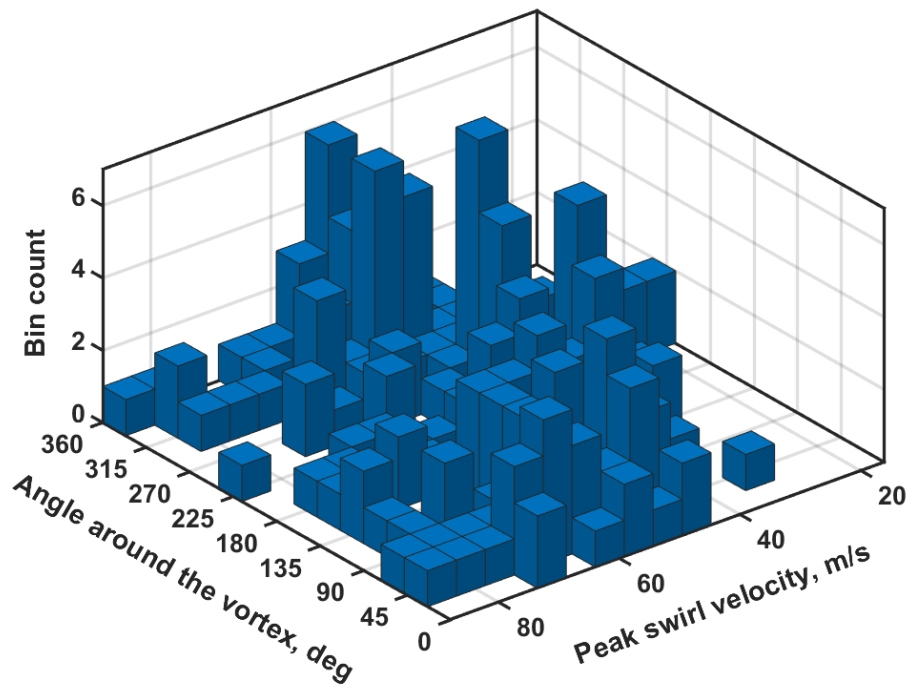
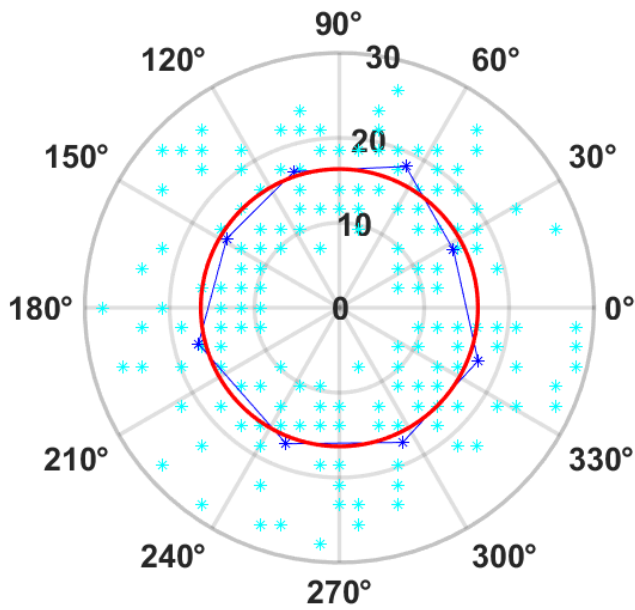
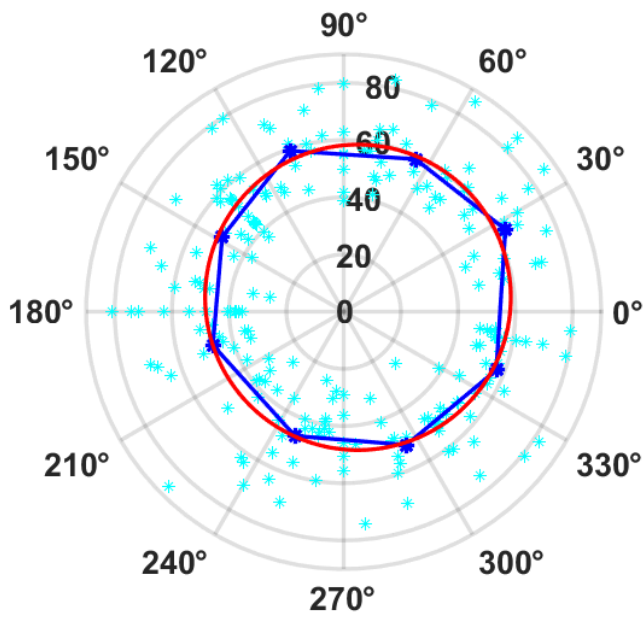


Figure B5. Histogram showing the peak swirl velocity around the vortex.



(a) Mean core radius, mm



(b) Mean peak swirl velocity, m/s

Figure B6. Core radius and swirl velocity distribution around the vortex- $\theta_0 = 12^\circ$, $\psi = 150^\circ$.

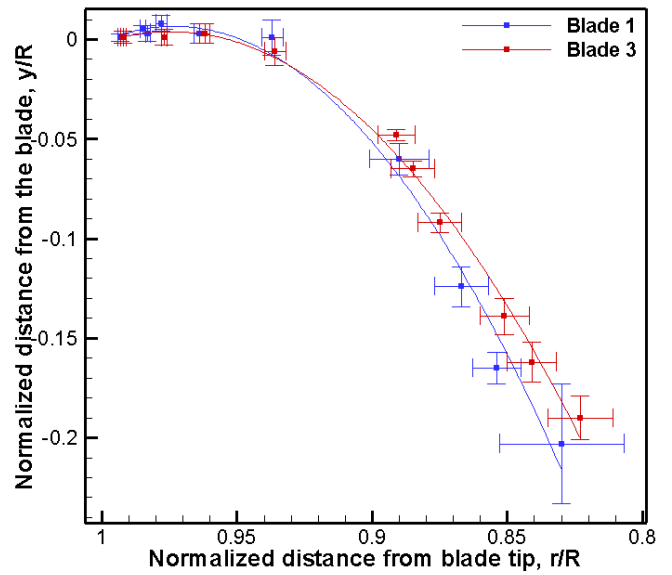


Figure C1. Blade to blade comparison at $\theta_0 = 8^\circ$.

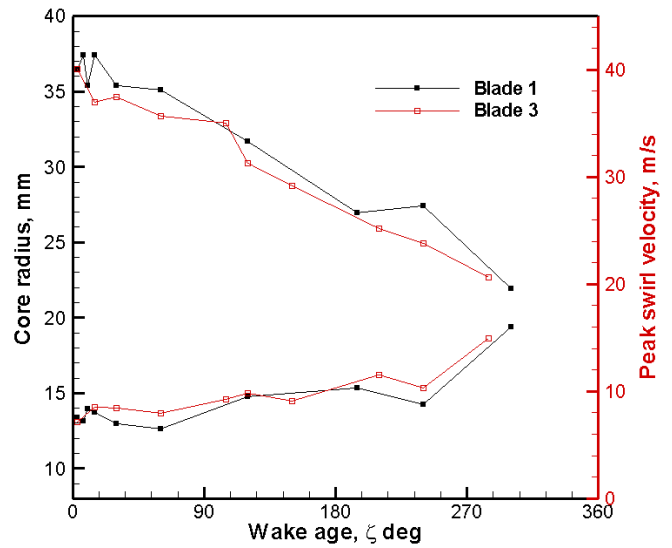


Figure C2. Blade to blade comparison of core properties at $\theta_0 = 8^\circ$.